

Efficient Transformer-Inspired Variants of Physics-Informed Deep Operator Networks*

Zhi-Feng Wei^{†1}, Wenqian Chen^{‡1}, and Panos Stinis^{§1,2,3}

¹*Advanced Computing, Mathematics, and Data Division, Pacific Northwest National Laboratory, Richland, WA 99354, USA*

²*Department of Applied Mathematics, University of Washington, Seattle, WA 98195, USA*

³*Division of Applied Mathematics, Brown University, Providence, RI 02912, USA*

Abstract

Operator learning has emerged as a promising tool for accelerating the solution of partial differential equations (PDEs). The Deep Operator Networks (DeepONets) represent a pioneering framework in this area: the “vanilla” DeepONet is valued for its simplicity and efficiency, while the modified DeepONet achieves higher accuracy at the cost of increased training time. In this work, we propose a series of *Transformer-inspired* DeepONet variants that introduce bidirectional cross-conditioning between the branch and trunk networks in DeepONet. Query-point information is injected into the branch network and input-function information into the trunk network, enabling dynamic dependencies while preserving the simplicity and efficiency of the “vanilla” DeepONet in a non-intrusive manner. Experiments on four PDE benchmarks—advection, diffusion–reaction, Burgers’, and Korteweg–de Vries equations—show that for each case, there exists a variant that matches or surpasses the accuracy of the modified DeepONet while offering improved training efficiency. Moreover, the best-performing variant for each equation aligns naturally with the equation’s underlying characteristics, suggesting that the effectiveness of cross-conditioning depends on the characteristics of the equation and its underlying physics. To ensure robustness, we validate the effectiveness of our variants through a range of rigorous statistical analyses, among them the Wilcoxon Two One-Sided Test, Glass’s Delta, and Spearman’s rank correlation.

Keywords: Physics-Informed Operator Learning, Deep Operator Networks, Transformer-Inspired Architectures, Partial Differential Equations

*Current version: September 3, 2025. Typeset with ♥ and L^AT_EX.

[†]Email: zfwei@pnnl.gov.

[‡]Email: wenqian.chen@pnnl.gov.

[§]Email: panagiotis.stinis@pnnl.gov.

Contents

1	Introduction	1
2	Technical Approach	2
2.1	Physics-Informed DeepONet	3
2.2	Transformer-Inspired DeepONet Variants	5
3	Numerical Results	10
3.1	Advection Equation	10
3.2	Diffusion–Reaction Equation	13
3.3	Burgers’ Equation	16
3.4	Korteweg–de Vries Equation	23
4	Discussion and Conclusion	26
	Code and Data Availability	26
	Acknowledgement	26
A	Data Generation and Network Parameters	27
A.1	Data Generation	27
A.2	Network Parameters	28
B	Supporting Data and Extended Results	30
B.1	Raw Data Underlying Figures	30
B.2	Reference-Prediction Comparisons and Discussion	33
B.3	Results Reported in the Literature	41
C	Rigorous Statistical Analysis Procedures	42
C.1	Percentage of Negative Difference	42
C.2	Wilcoxon Two One-Sided Tests (TOST) for Equivalence	42
C.3	Determining the Model with Better Accuracy if Inequivalent	45
C.4	Quantifying the Accuracy Difference	45
C.5	Behavioral Correlation of the Models	45
C.6	Statistical Analysis Results	47
D	Symbols & Notation	48
	References	48

1 Introduction

Partial differential equations (PDEs) play a central role in modeling physical, engineering, and biological phenomena. They govern a wide spectrum of processes, such as fluid dynamics, chemical reactions, and wave propagation [Evans 2022]. While classical numerical solvers for PDEs are accurate, they become computationally prohibitive in high-dimensional or parameterized settings [E and B. Yu 2018; Han et al. 2018; Hesthaven et al. 2016; Quarteroni et al. 2015]. To overcome these challenges, *operator learning* has emerged as a promising alternative [Boullé and Townsend 2024; Zongyi Li et al. 2020; Lu et al. 2021]. By training neural networks to approximate solution operators, this approach enables fast and flexible inference after training. Moreover, *physics-informed training strategies* reduce reliance on large datasets and maintain performance in data-scarce regimes [Raissi et al. 2019], though improving their convergence remains an active area of research [W. Chen et al. 2025; Howard et al. 2025; Krishnapriyan et al. 2021; S. Wang and Perdikaris 2023; S. Wang, X. Yu et al. 2022].

As a pioneering operator learning framework, the Deep Operator Network (hereafter referred to as “vanilla” DeepONet) demonstrated the potential of neural operators for solving PDEs [Lu et al. 2021; S. Wang, H. Wang et al. 2021]. It consists of two distinct subnetworks: a *branch network* that encodes the input function (e.g., the initial condition or source term) and a *trunk network* that encodes the query spatiotemporal point. These two components operate independently during inference, which, while structurally elegant, can limit the model’s ability to capture complex interactions between input function and query point [Kovachki et al. 2023]. In response to this architectural limitation, various extensions have been proposed to improve representational capacity, including SVD-DeepONet [Venturi and Casey 2023], the R-adaptive DeepONet designed for discontinuities [Zhu et al. 2024], multi-input EDeepONet [Tan and L. Chen 2022], and the Separable Operator Networks [X. Yu et al. 2024]. These models reflect an active line of research focused on enhancing DeepONet’s expressive capacity through architectural innovations. Specifically, to improve the predictive accuracy of the “vanilla” DeepONet, a modified DeepONet architecture with increased structural complexity was proposed in prior work [S. Wang, H. Wang et al. 2022]. While this design demonstrates improved predictive accuracy across a range of PDE benchmarks, it typically requires two to three times longer training time. The original “vanilla” DeepONet, on the other hand, remains attractive for its computational simplicity. These contrasting approaches reflect an important trade-off between accuracy and efficiency. Motivated by these developments, we aim to explore architectural enhancements that build on existing insights—drawing inspiration from the attention mechanism in Transformers—to improve *accuracy* while preserving *efficiency*.

The Transformer architecture has revolutionized sequence modeling in natural language processing by capturing long-range dependencies through the attention mechanism [Vaswani et al. 2017]. This capacity to model both long-range and cross-input dependencies has also made attention mechanisms appealing for operator learning, where interactions between input functions and query spatiotemporal points are crucial. Motivated by this, several studies have

introduced Transformers or attention-based modules into PDE operator learning, such as the operator transformer [Zijie Li et al. 2022], LOCA architecture with coupled attention [Kissas et al. 2022], Position-induced Transformer [J. Chen and Wu 2024], the GNOT architecture for multiple input functions and irregular meshes [Hao et al. 2023], and the use of transformers for differential equations with finite regularity [Shih et al. 2025]. These promising directions have significantly expanded the design space for operator learning. However, these approaches often come with increased architectural complexity, which may raise the cost of implementation and training in practice. In this work, we explore a complementary approach focused on non-intrusive dependency modeling, aiming to retain simplicity and efficiency.

Building on the observation that the “vanilla” DeepONet lacks *cross-dependence between its two subnetworks*—the branch network depends solely on the input function, while the trunk network depends solely on the query spatiotemporal point—and that there is *no communication* or exchange of information between them, we propose Transformer-inspired DeepONet variants. Motivated by attention mechanisms [Phuong and Hutter 2022; Vaswani et al. 2017], we introduce query-point information into the branch network, enabling its output to vary dynamically with respect to the query point. Conversely, we provide the trunk network with information from the input function, allowing its outputs to better capture the underlying problem context. These modifications establish *bidirectional interaction* between the branch and trunk networks. The design remains *dependency-driven*, *non-intrusive*, and *architecturally simple*. As a result, the proposed variants retain the training efficiency of the “vanilla” DeepONet while achieving predictive accuracy comparable to or even exceeding that of the modified DeepONet, with minimal added complexity. We demonstrate the effectiveness of our approach through evaluations on four PDE benchmarks: advection, diffusion–reaction, Burgers’, and Korteweg–de Vries equations. To ensure the robustness of our findings, we apply rigorous statistical tools—including the Wilcoxon Two One-Sided Test (TOST), Glass’s Delta, and Spearman’s rank correlation ρ —to compare the predictive accuracy of the proposed model variants.

The remainder of this paper is organized as follows. Section 2 presents the key technical background and describes the architecture of our Transformer-inspired DeepONet variants in detail. Section 3 reports numerical results on four PDE benchmarks. Section 4 offers discussion and concluding remarks. Finally, the appendices detail data generation procedures, model training settings, raw results, and the rigorous statistical analysis methods used to support our findings.

2 Technical Approach

This section introduces the architectures of the operator learning models investigated in this study. We first describe the foundational “vanilla” DeepONet [Lu et al. 2021; S. Wang, H. Wang et al. 2021] and modified DeepONet [S. Wang, H. Wang et al. 2022] frameworks in Section 2.1. Building upon these concepts, Section 2.2 then details the structure of our proposed Transformer-inspired DeepONet variants.

We consider *time-dependent* partial differential equations (PDEs), where certain properties of the system are allowed to vary. These properties, represented by input functions, can define the initial conditions or source terms. To formalize this problem, let $(\mathcal{U}, \mathcal{V}, \mathcal{S})$ be a triplet of Banach spaces. A general time-dependent PDE can be expressed with a linear or nonlinear operator $\mathcal{N}: \mathcal{U} \times \mathcal{S} \rightarrow \mathcal{V}$ as:

$$\mathbf{s}_t + \mathcal{N}(\mathbf{u}, \mathbf{s}) = 0, \quad (1)$$

where $\mathbf{u} \in \mathcal{U}$ is the input function and $\mathbf{s} \in \mathcal{S}$ is the corresponding unknown solution. In the concrete PDEs considered later, \mathbf{u} typically represents the initial condition, coefficient, or a source term; in such cases, $\mathbf{u}(\mathbf{x})$ and the solution $\mathbf{s}(t, \mathbf{x})$ share the same spatial domain. We assume that for any given $\mathbf{u} \in \mathcal{U}$, a unique solution \mathbf{s} exists under appropriate initial and boundary conditions. The solution operator $G: \mathcal{U} \rightarrow \mathcal{S}$ is thus defined as

$$G(\mathbf{u}) := \mathbf{s}. \quad (2)$$

Here, the solution $\mathbf{s} = \mathbf{s}(t, \mathbf{x})$ is a function of both time t and spatial coordinates \mathbf{x} , while the input function $\mathbf{u} = \mathbf{u}(\mathbf{x})$ is a function of the spatial coordinates only.

2.1 Physics-Informed DeepONet

To approximate the solution operator G , the “vanilla” DeepONet framework can be employed [Lu et al. 2021]. As illustrated in Figure 1, a “vanilla” DeepONet consists of two distinct neural networks: a “branch network” and a “trunk network”.

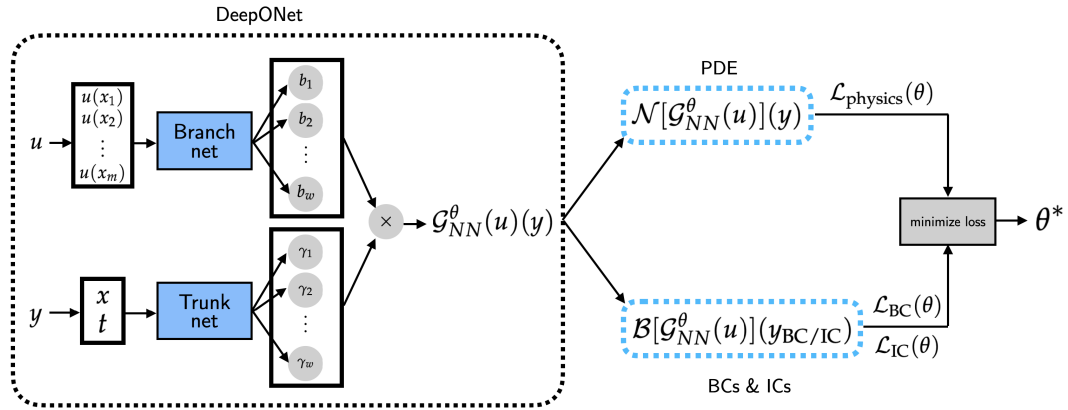


Figure 1: Physics-informed “vanilla” DeepONet (From [Williams et al. 2024]).

The branch net processes the input function \mathbf{u} . Specifically, it takes a discrete representation of \mathbf{u} , evaluated at a fixed set of sensor spatial locations $\{\mathbf{x}_i\}_{i=1}^m$, and produces a feature embedding $(b_1, b_2, \dots, b_w)^\top \in \mathbb{R}^w$. The trunk net takes the continuous spatiotemporal coordinates $\mathbf{y} = (t, \mathbf{x})$ as input and generates a corresponding feature embedding $(\gamma_1, \gamma_2, \dots, \gamma_w)^\top \in \mathbb{R}^w$. The final prediction is formed by computing the inner product of these two embeddings. The

output of the “vanilla” DeepONet, representing the solution \mathbf{s} for a given function \mathbf{u} , evaluated at spatiotemporal coordinates $\mathbf{y} = (t, \mathbf{x})$, is expressed as:

$$G^{\theta}(\mathbf{u})(\mathbf{y}) = \sum_{k=1}^w \underbrace{b_k(\mathbf{u}(\mathbf{x}_1), \mathbf{u}(\mathbf{x}_2), \dots, \mathbf{u}(\mathbf{x}_m))}_{\text{branch net}} \underbrace{\gamma_k(\mathbf{y})}_{\text{trunk net}}, \quad (3)$$

where θ represents the collection of all trainable parameters in both branch net and trunk net.

The key insight behind *physics-informed* “vanilla” DeepONets [S. Wang, H. Wang et al. 2021] is that the model output is differentiable with respect to its spatiotemporal input coordinates $\mathbf{y} = (t, \mathbf{x})$. This property allows the use of automatic differentiation to compute the derivatives of the predicted solution \mathbf{s} , which can then be substituted into the governing PDE (Equation (1)) to construct a residual loss term. By minimizing this physics-based residual, together with the losses associated with the initial and boundary conditions, the network can be trained to satisfy the underlying physical laws without requiring labeled solution data. In physics-informed training, multiple loss terms are typically combined, and their relative weights must be tuned to achieve rapid and stable convergence. To address this loss-balancing challenge, we employ both a moderately localized conjugate kernel (CK) weighting strategy (see [Qadeer et al. 2023; S. Wang, H. Wang et al. 2022]) and the balanced-residual-decay-rate (BRDR) self-adaptive weighting scheme [W. Chen et al. 2025] in our numerical experiments.

In [S. Wang, H. Wang et al. 2022], an improved architecture called the “modified DeepONet” was proposed, as illustrated in Figure 2. This architecture retains the “vanilla” DeepONet as a backbone but incorporates two additional encoders and modifies the forward pass. While these changes reportedly lead to more accurate predictions, they also incur longer training times due to increased structural complexity.

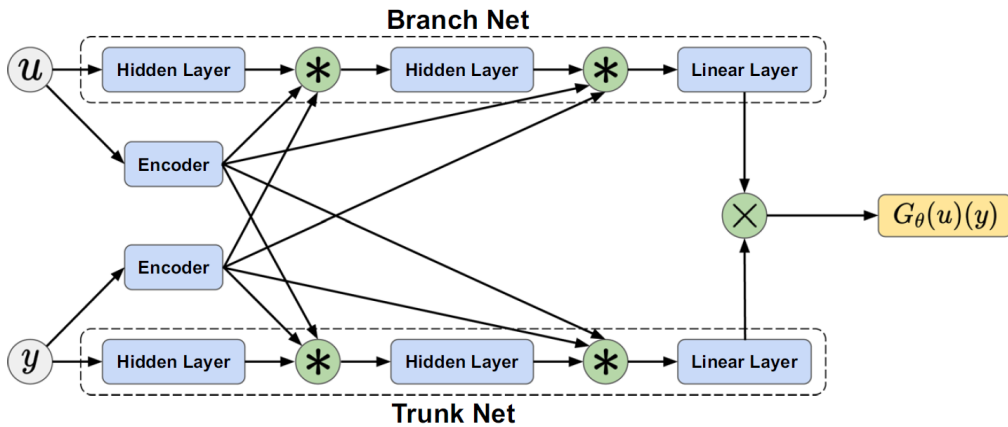


Figure 2: The modified DeepONet architecture (From [S. Wang, H. Wang et al. 2022]).

2.2 Transformer-Inspired DeepONet Variants

The trade-off between predictive accuracy and computational cost inherent in the existing “vanilla” DeepONet and the modified DeepONet frameworks motivates our work. The modified DeepONet, as introduced in [S. Wang, H. Wang et al. 2022], exhibits superior predictive accuracy in solving PDEs. However, compared to the “vanilla” DeepONet, it imposes significantly higher training costs, particularly when dealing with higher-order PDEs, with training times often increasing by a factor of two or three (see comparison in Section 3). To address this challenge, we propose a series of Transformer-inspired variants built upon the “vanilla” DeepONet architecture. Our primary objective is to develop models that not only retain the predictive enhancements of the modified DeepONet but also preserve the training efficiency and structural simplicity inherent to the “vanilla” DeepONet framework.

Before detailing our proposed models, we first briefly review the attention mechanism, the key component of the standard Transformer architecture, originally introduced in [Vaswani et al. 2017]. Readers seeking a self-contained and mathematically precise overview of Transformer architectures and algorithms are referred to [Phuong and Hutter 2022].

2.2.1 The Transformer Self-Attention Mechanism

The main architectural component of the Transformer is the attention mechanism. Algorithm 1 provides the details of a basic single-query attention mechanism. In accordance with common mathematical conventions, the algorithm assumes that matrices act on column vectors placed to their right through left multiplication.

In this attention mechanism, the attention output $\tilde{\mathbf{v}}$ for the current token \mathbf{e} is computed as a weighted sum of the value vectors $\{\mathbf{v}_\tau\}_{\tau=1}^T$, each of which is obtained by applying a linear transformation to the corresponding context token \mathbf{e}_τ . The weights $\{\alpha_\tau\}_{\tau=1}^T$, known as attention scores, serve as the combination coefficients for the value vectors $\{\mathbf{v}_\tau\}_{\tau=1}^T$. As such, α_τ directly determines the contribution of each context token to the final representation. These scores are computed via scaled dot-product, which measures the compatibility between the query vector \mathbf{q} of the current token and the key vectors $\{\mathbf{k}_\tau\}_{\tau=1}^T$ of the context tokens.

2.2.2 Relating Transformer Attention to DeepONet

By comparing the output formulations of the “vanilla” DeepONet and the attention mechanism (Algorithm 1) used in Transformer, we can establish a conceptual correspondence. Both architectures compute an output as a linear combination of basis functions.

In the DeepONet framework, the trunk net outputs, $\{\gamma_k(\mathbf{y})\}_{k=1}^w$, serve as the basis functions [Meuris et al. 2023], where $\mathbf{y} = (t, \mathbf{x})$ is the spatiotemporal coordinates. The corresponding coefficients, $\{b_k\}_{k=1}^w$, are generated by the branch net. The input to the branch net—the discrete function representation $\{\mathbf{u}(\mathbf{x}_i)\}_{i=1}^m$ —can be viewed as the set of context tokens, as it provides the necessary context for the specific PDE instance. However, the resulting coefficients $\{b_k\}_{k=1}^w$ remain static with respect to $\mathbf{y} = (t, \mathbf{x})$ and do not dynamically adapt to specific

Algorithm 1 Basic single-query attention (From [Phuong and Hutter 2022]).

Input: $\mathbf{e} \in \mathbb{R}^{d_{\text{in}}}$ ▷ vector representation of the current token
Input: $\{\mathbf{e}_\tau\}_{\tau=1}^T \subseteq \mathbb{R}^{d_{\text{in}}}$ ▷ vector representations of context tokens
Output: $\tilde{\mathbf{v}} \in \mathbb{R}^{d_{\text{out}}}$ ▷ attention output

- 1: **Parameters:**
- 2: $\mathbf{W}_q, \mathbf{W}_k \in \mathbb{R}^{d_{\text{attn}} \times d_{\text{in}}}, \quad \mathbf{b}_q, \mathbf{b}_k \in \mathbb{R}^{d_{\text{attn}}}$
- 3: $\mathbf{W}_v \in \mathbb{R}^{d_{\text{out}} \times d_{\text{in}}}, \quad \mathbf{b}_v \in \mathbb{R}^{d_{\text{out}}}$
- 4: $\mathbf{q} \leftarrow \mathbf{W}_q \mathbf{e} + \mathbf{b}_q$
- 5: **for** $\tau = 1$ to T **do**
- 6: $\mathbf{k}_\tau \leftarrow \mathbf{W}_k \mathbf{e}_\tau + \mathbf{b}_k$
- 7: $\mathbf{v}_\tau \leftarrow \mathbf{W}_v \mathbf{e}_\tau + \mathbf{b}_v$
- 8: **end for**
- 9: **for** $\tau = 1$ to T **do**
- 10: $\alpha_\tau \leftarrow \frac{\exp(\mathbf{q}^\top \mathbf{k}_\tau / \sqrt{d_{\text{attn}}})}{\sum_{\tau=1}^T \exp(\mathbf{q}^\top \mathbf{k}_\tau / \sqrt{d_{\text{attn}}})}$
- 11: **end for**
- 12: $\tilde{\mathbf{v}} \leftarrow \sum_{\tau=1}^T \alpha_\tau \mathbf{v}_\tau$
- 13: **return** $\tilde{\mathbf{v}}$

query points.

In contrast, the attention mechanism in Transformers introduces a dynamic dependency on the query point. Here, the value vectors $\{\mathbf{v}_\tau\}_{\tau=1}^T$, derived from linear transformations of the context tokens $\{\mathbf{e}_\tau\}_{\tau=1}^T$, act as basis functions. The coefficients $\{\alpha_\tau\}_{\tau=1}^T$ are computed dynamically based on the compatibility between the query vector \mathbf{q} of the current token \mathbf{e} and the key vectors $\{\mathbf{k}_\tau\}_{\tau=1}^T$, enabling the model to adapt to specific query points.

This comparison reveals two fundamental distinctions:

1. **Query-Dependent Coefficients:** Transformers compute the coefficients $\{\alpha_\tau\}_{\tau=1}^T$ dynamically, allowing them to adjust based on the query vector \mathbf{q} . In the “vanilla” DeepONet framework, the coefficients $\{b_k\}_{k=1}^w$ remain static for a given input \mathbf{u} and cannot adapt to variations in the query point $\mathbf{y} = (t, \mathbf{x})$.
2. **Role of the Input “Context” Function:** In Transformers, the context tokens $\{\mathbf{e}_\tau\}_{\tau=1}^T$ interact with both the basis functions $\{\mathbf{v}_\tau\}_{\tau=1}^T$ and the coefficients $\{\alpha_\tau\}_{\tau=1}^T$, creating a bidirectional dependency. In contrast, in the “vanilla” DeepONet framework, the input “context” function \mathbf{u} solely determines the coefficients $\{b_k\}_{k=1}^w$, without any direct influence on the basis functions $\{\gamma_k(\mathbf{y})\}_{k=1}^w$.

These observations underscore fundamental limitations in the expressive power of the “vanilla” DeepONet architecture. Specifically, the static nature of its query-independent coefficients and the rigid separation of functional roles between the branch and trunk nets restrict its capacity to effectively model complex operator mappings with dynamic dependencies.

To overcome these challenges, our proposed Transformer-inspired variants introduce dynamic query dependence and expand the influence of input “context” functions, establishing a dynamic coupling between basis functions and coefficients.

2.2.3 Proposed Dependency-Enhanced Architectures

Based on the analysis above, we introduce a series of architectural variants that enhance the “vanilla” DeepONet framework by incorporating query-dependent coefficients that enable branch net computations to dynamically adjust to specific spatiotemporal query points, along with trunk-side conditioning on the input “context” function to directly influence the basis functions. Recall that, for time-dependent PDEs considered in this study, the input function $\mathbf{u}(\mathbf{x})$ and the corresponding solution $\mathbf{s}(t, \mathbf{x})$ share the same spatial domain.

T-DeepONet–Bx (Query-Dependent Branch Net). To address the first limitation in the “vanilla” DeepONet architecture, we introduce a variant by injecting the spatial coordinate \mathbf{x} as an additional input to the branch net. This modification enables the coefficients of the basis functions to dynamically depend on query points, reflecting the adaptive nature of attention scores in a Transformer. As such, this variant, referred to as T-DeepONet–Bx (Bx), incorporates \mathbf{x} directly into the branch net. The branch net computes the query-dependent coefficients $\mathbf{b} = \mathbf{b}(\mathbf{u}, \mathbf{x})$, and the model output is formulated as:

$$G^\theta(\mathbf{u})(t, \mathbf{x}) = \sum_{k=1}^w b_k(\mathbf{u}, \mathbf{x}) \gamma_k(t, \mathbf{x}). \quad (4)$$

T-DeepONet–TL (Context-Aware Trunk Net). To address the second limitation in the “vanilla” DeepONet architecture, this variant introduces dependency of the trunk net on the input “context” function \mathbf{u} . Similar to how value vectors $\{\mathbf{v}_\tau\}_{\tau=1}^T$ in a Transformer are influenced by context tokens $\{\mathbf{e}_\tau\}_{\tau=1}^T$, the trunk net in T-DeepONet–TL takes both the query point (t, \mathbf{x}) and the value of the input function at the specific spatial coordinate, $\mathbf{u}(\mathbf{x})$, as inputs. Consequently, the basis functions are defined as $\gamma = \gamma(t, \mathbf{x}, \mathbf{u}(\mathbf{x}))$. This variant is referred to as T-DeepONet–TL (TL), emphasizing that the trunk net conditions on the local value $\mathbf{u}(\mathbf{x})$ to enhance its representation capabilities. The model output is expressed as:

$$G^\theta(\mathbf{u})(t, \mathbf{x}) = \sum_{k=1}^w b_k(\mathbf{u}) \gamma_k(t, \mathbf{x}, \mathbf{u}(\mathbf{x})). \quad (5)$$

T-DeepONet–BxTL (Combined Local Context). This variant integrates the principles of the first two architectures. Specifically, the branch net exhibits query-dependency, dynamically adapting its coefficients to the spatial input \mathbf{x} , while the trunk net introduces context-awareness by conditioning on the local value $\mathbf{u}(\mathbf{x})$ of the input function. We refer to this variant as T-DeepONet–BxTL (BxTL), denoting branch-side injection of \mathbf{x} and trunk-side

local conditioning. The final model output is formulated as:

$$G^\theta(\mathbf{u})(t, \mathbf{x}) = \sum_{k=1}^w b_k(\mathbf{u}, \mathbf{x}) \gamma_k(t, \mathbf{x}, \mathbf{u}(\mathbf{x})). \quad (6)$$

T-DeepONet-BxTG (Combined Global Context). Building on the architecture of T-DeepONet-BxTL, this variant introduces a more general framework by allowing the trunk net to access the entire input function \mathbf{u} . This modification equips the trunk net with global context when generating the basis functions, enhancing its ability to capture dependencies across the spatial domain. We refer to this variant as T-DeepONet-BxTG (BxTG), highlighting the use of global context rather than restricting to the local value $u(\mathbf{x})$. The model output is expressed as:

$$G^\theta(\mathbf{u})(t, \mathbf{x}) = \sum_{k=1}^w b_k(\mathbf{u}, \mathbf{x}) \gamma_k(t, \mathbf{x}, \mathbf{u}). \quad (7)$$

In this formulation, both the basis functions and their coefficients are directly influenced by the global context of the input function \mathbf{u} and the specific query point (t, \mathbf{x}) . This global integration allows the trunk and branch nets to share richer contextual information, facilitating enhanced expressiveness in modeling complex operator mappings. This approach aligns with the philosophy of the modified DeepONet architecture [S. Wang, H. Wang et al. 2022], which similarly promotes information exchange between the branch net and the trunk net. However, T-DeepONet-BxTG achieves this through a straightforward implementation of dependency mechanisms inspired by the dynamic interactions in Transformer attention, enabling simultaneous integration of global context and query-specific features.

T-DeepONet-TF (Context-Aware Trunk Net with Fourier Coefficients). For PDEs with periodic boundary conditions, where the input function \mathbf{u} (as the initial condition) is often periodic, we leverage a compact representation of \mathbf{u} using its truncated Fourier coefficients $\hat{\mathbf{u}}_\Lambda := (\hat{u}_k)_{k \in \Lambda}$. Here, Λ represents a low-frequency index set, which will be specified for each equation. These coefficients provide a global frequency-based summary of \mathbf{u} .

Building on T-DeepONet-TL, this variant incorporates these Fourier coefficients directly into the trunk net. The trunk net takes the query point (t, \mathbf{x}) and the Fourier coefficients $\hat{\mathbf{u}}_\Lambda$ as input to generate the basis functions, formulated as $\gamma = \gamma(t, \mathbf{x}, \hat{\mathbf{u}}_\Lambda)$. We refer to this variant as T-DeepONet-TF (TF), highlighting the trunk's ability to utilize Fourier-based global context. The model output is expressed as:

$$G^\theta(\mathbf{u})(t, \mathbf{x}) = \sum_{k=1}^w b_k(\mathbf{u}) \gamma_k(t, \mathbf{x}, \hat{\mathbf{u}}_\Lambda). \quad (8)$$

This design equips the trunk net with global frequency information about the input function, making it particularly effective for capturing the behavior of solutions subject to periodic boundary conditions.

T-DeepONet–BxTF (Combined Global Context with Fourier Coefficients). Extending the principles of T-DeepONet–TF, this variant builds upon T-DeepONet–BxTL by incorporating a truncated set of Fourier coefficients $\hat{\mathbf{u}}_\Lambda$ to represent the global context, rather than relying solely on the local context $\mathbf{u}(\mathbf{x})$. In this architecture, the branch net computes the coefficients $\{b_k\}_{k=1}^w$, which depend on the input function \mathbf{u} and the spatial query coordinate \mathbf{x} . Simultaneously, the trunk net generates basis functions informed by the global frequency content encoded in the Fourier coefficients $\hat{\mathbf{u}}_\Lambda$.

This variant, referred to as T-DeepONet–BxTF (BxTF), highlights the integration of branch-side spatial information with trunk-side frequency-aware conditioning. The model output is expressed as:

$$G^\theta(\mathbf{u})(t, \mathbf{x}) = \sum_{k=1}^w b_k(\mathbf{u}, \mathbf{x}) \gamma_k(t, \mathbf{x}, \hat{\mathbf{u}}_\Lambda). \quad (9)$$

This design allows the model to dynamically adjust the weights of its frequency-aware basis functions based on spatial query points, thereby enhancing its flexibility to effectively handle PDEs with periodic boundary conditions.

Table 1: Summary of Architectural Variants and Their Input Features. The second and third columns list the feature sets fed to the branch net and trunk net, respectively. Notation: \mathbf{u} denotes the input “context” function (sampled at sensor points); $t \in \mathbb{R}$ is the temporal coordinate and $\mathbf{x} \in \mathbb{R}^d$ the spatial coordinates; $\mathbf{u}(\mathbf{x})$ is the value of \mathbf{u} at spatial location \mathbf{x} ; $\hat{\mathbf{u}}_\Lambda$ denotes the truncated Fourier coefficients.

Variant	Branch input	Trunk input
“vanilla” DeepONet	\mathbf{u}	t, \mathbf{x}
modified DeepONet	\mathbf{u}	t, \mathbf{x}
T-DeepONet–Bx	\mathbf{u}, \mathbf{x}	t, \mathbf{x}
T-DeepONet–TL	\mathbf{u}	$t, \mathbf{x}, \mathbf{u}(\mathbf{x})$
T-DeepONet–BxTL	\mathbf{u}, \mathbf{x}	$t, \mathbf{x}, \mathbf{u}(\mathbf{x})$
T-DeepONet–BxTG	\mathbf{u}, \mathbf{x}	$t, \mathbf{x}, \mathbf{u}$
T-DeepONet–TF	\mathbf{u}	$t, \mathbf{x}, \hat{\mathbf{u}}_\Lambda$
T-DeepONet–BxTF	\mathbf{u}, \mathbf{x}	$t, \mathbf{x}, \hat{\mathbf{u}}_\Lambda$

A summary of our Transformer-inspired DeepONet variants is presented in Table 1. These designs are intentionally kept *dependency-driven*, *non-intrusive*, and *architecturally simple*, ensuring that they preserve the training efficiency of the original “vanilla” DeepONet while introducing only minimal additional complexity.

Having outlined the theoretical motivations and architectural details of the proposed DeepONet variants, we now shift our focus to their empirical evaluation. In the next section, we will conduct a comprehensive performance comparison against both the “vanilla” DeepONet and

the modified DeepONet models, highlighting the advancements in accuracy and computational efficiency achieved by our variants across multiple benchmark problems.

3 Numerical Results

In this section, we present numerical results for four PDEs: the advection equation, the diffusion–reaction equation, Burgers’ equation with varying viscosity, and the Korteweg–de Vries equation. We compare the performance of the “vanilla” DeepONet, the modified DeepONet, and the Transformer-inspired variants described in Section 2. The experiments assess both predictive accuracy and training efficiency, using rigorous statistical methods outlined in Appendix C.

The experimental setup follows prior work: [S. Wang, H. Wang et al. 2022] for the advection and Burgers’ equations, [S. Wang, H. Wang et al. 2021] for the diffusion–reaction equation, and [Williams et al. 2024] for the KdV equation. For each PDE, we adopt whichever loss-weighting scheme (CK or BRDR) yields better accuracy, and also test deterministic and random Fourier feature embeddings. Reported metrics are averaged over multiple runs with different random seeds to mitigate stochastic variability. Further implementation details are provided in Appendix A, while the raw data underlying figures, prediction–reference visualizations, and selected literature comparisons are collected in Appendices B.1 to B.3.

3.1 Advection Equation

We first consider a one-dimensional linear advection equation with spatially varying coefficients, given by

$$\frac{\partial s}{\partial t} + u(x) \frac{\partial s}{\partial x} = 0, \quad (t, x) \in (0, 1) \times (0, 1), \quad (10)$$

subject to the initial condition

$$s(0, x) = f(x), \quad x \in [0, 1], \quad (11)$$

and the boundary condition

$$s(t, 0) = g(t), \quad t \in [0, 1], \quad (12)$$

where $f(x) = \sin \pi x$ and $g(t) = \sin \frac{\pi t}{2}$. To ensure numerical stability, the advection velocity $u(x)$ is enforced to be strictly positive by defining

$$u(x) = v(x) - \min_x v(x) + 1, \quad (13)$$

where $v(x)$ is drawn from a Gaussian random field (GRF) with correlation length $l = 0.2$. The learning objective is to approximate the solution operator G that maps the spatially varying coefficient $u(x)$ to the corresponding spatiotemporal solution $s(t, x)$.

The performance of all evaluated models is summarized in Figures 3 to 5. The modified DeepONet (black star marker in Figure 3) serves as the reference for both training time and accuracy. Among the Transformer-inspired variants, Variant BxTG (gold marker in Figure 3) achieves the lowest mean relative L^2 error among the faster models, offering a speedup of nearly 45% in average per-iteration training time over multiple random seeds, while maintaining comparable accuracy (mean relative L^2 error 0.925% for BxTG and 0.926% for the modified DeepONet). As an illustrative example, the convergence curves for one training run in Figure 4 show that Variant BxTG completes 300,000 training iterations in 2,929s, compared to 4,470s for the modified DeepONet, representing a substantial reduction of about 35% in the total time to complete the full training budget and a similar prediction accuracy. However, the time required for the mean relative L^2 error to stabilize near its optimal value is only marginally shorter for Variant BxTG in this case, in contrast to other PDE problems discussed later (e.g., Burgers' equation), where both total training time and stabilization time show pronounced improvements. The strong performance of Variant BxTG can likely be attributed to its architectural modification that incorporates the full velocity field $u(x)$ directly into the trunk network input. In advection-dominated problems, the solution at each spatiotemporal location is largely determined by the transport of initial information along characteristic curves governed by the ordinary differential equation $\frac{dx}{dt} = u(x)$. Providing the entire profile of $u(x)$ —rather than only its local value at the evaluation point—allows the model to capture long-range dependencies and better infer the characteristic trajectories that underlie the transport behavior. This global encoding of the velocity field aligns naturally with the hyperbolic nature of the advection equation and enhances the model's ability to resolve directional propagation patterns, thereby contributing to improved predictive accuracy. Additionally, the relatively simple architecture of our variants contributes to shorter training times. Error distributions over multiple test instances (Figure 5) show that Variant BxTG has a slightly lower median relative L^2 error of 0.85% than 0.88% for the modified DeepONet, with similar spread. In test cases, Variant BxTG achieved better predictive accuracy in 57.00% of cases compared to the modified DeepONet. A non-parametric Wilcoxon two one-sided tests (TOST) for equivalence (see Appendix C), with a margin of $\pm 0.1\%$, confirms that Variant BxTG and the modified DeepONet are statistically equivalent in predictive accuracy, while a high Spearman correlation coefficient ($\rho = 0.993$) indicates strong agreement in error patterns.

Overall: Variant BxTG delivers predictive accuracy statistically equivalent to that of the modified DeepONet, while achieving a substantial speedup in training time.

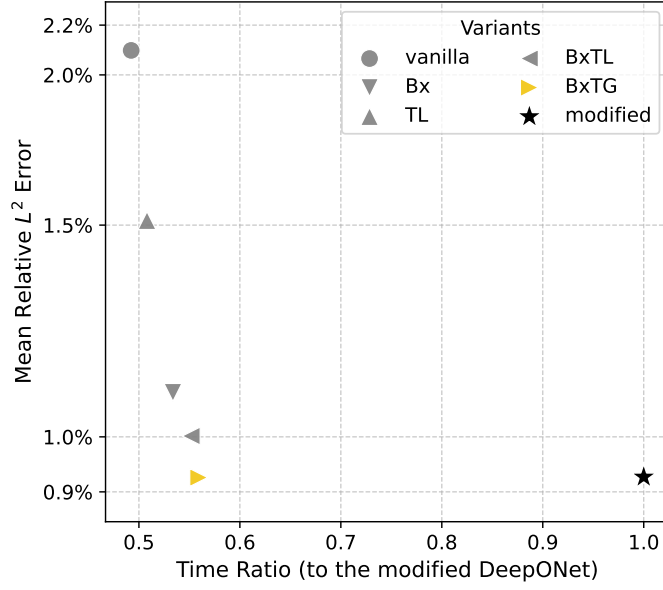


Figure 3: Performance comparison of model variants for the Advection equation. The horizontal axis shows the average per-iteration training time ratio relative to the modified DeepONet, averaged over multiple random seeds (lower is faster), while the vertical axis shows the mean relative L^2 error (lower is better). Marker shapes distinguish different model variants; the modified DeepONet is shown in black, and the best-performing variant is highlighted in gold.

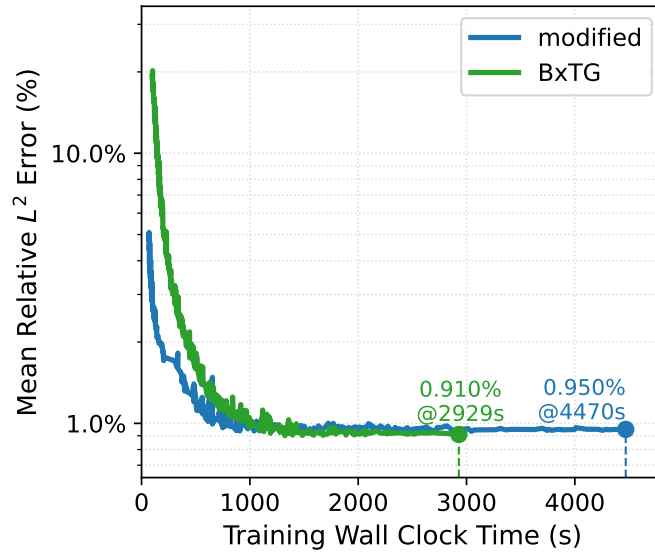


Figure 4: Comparison of training efficiency for the Advection equation. The horizontal axis shows the wall-clock training time for a single representative run, and the vertical axis shows the mean relative L^2 error over all test cases (log scale). Dashed vertical lines and annotations mark the time at which each model completed 300,000 training iterations.

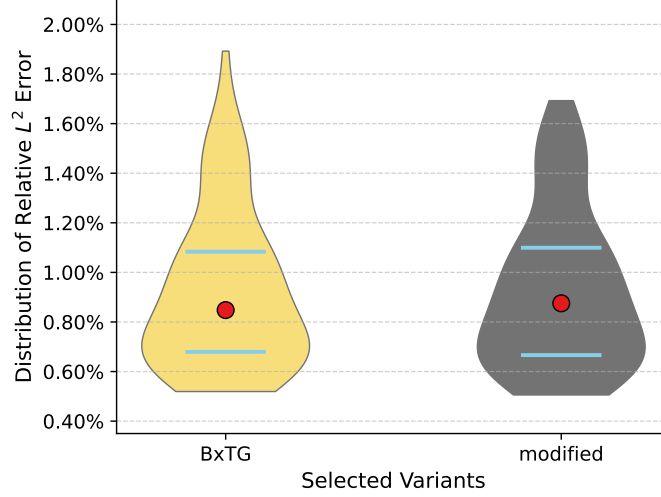


Figure 5: Distribution of relative L^2 errors for selected variants (gold: Variant BxTG; black: the modified DeepONet) on the Advection equation, evaluated over multiple random seeds and test instances. Horizontal bars span the interquartile range (25th to 75th percentile), and red dots mark the median.

3.2 Diffusion–Reaction Equation

We next consider a nonlinear diffusion–reaction equation with a spatially varying source term $u(x)$, formulated as

$$\frac{\partial s}{\partial t} = D \frac{\partial^2 s}{\partial x^2} + k s^2 + u(x), \quad (t, x) \in (0, 1] \times (0, 1], \quad (14)$$

subject to zero initial and boundary conditions:

$$s(0, x) = 0, \quad x \in [0, 1], \quad (15)$$

$$s(t, 0) = 0, \quad s(t, 1) = 0, \quad t \in [0, 1]. \quad (16)$$

Here, $D = 0.01$ denotes the diffusion coefficient and $k = 0.01$ the reaction rate. The objective is to learn the solution operator G that maps the source term $u(x)$ to the corresponding spatiotemporal solution $s(t, x)$.

The performance of all evaluated models is summarized in Figures 6 to 8. The modified DeepONet (black star marker in Figure 6) serves as the reference for both training time and accuracy. Among the Transformer-inspired variants, Variant TL (gold marker in Figure 6) achieves the lowest mean relative L^2 error among the faster models, offering an average per-iteration speedup of about 42% over multiple random seeds, while maintaining comparable accuracy as the modified DeepONet. As an illustrative example, the convergence curves for one training run in Figure 7 show that Variant TL completes 120,000 training iterations in 1,236 s, compared to 2,021 s for the modified DeepONet, representing a substantial reduction

of about 39% in the total time to complete the full training budget, alongside slightly improved accuracy. Moreover, at any given wall-clock time, the mean relative L^2 error of Variant TL (averaged over all test instances) remains consistently lower than that of the modified DeepONet, indicating faster convergence toward the optimum. The strong performance of Variant TL is likely attributable to its architectural simplification compared to the modified DeepONet, as well as the direct inclusion of the local value $u(x)$ of the source term into the trunk network, which appears explicitly in the PDE. By leveraging this structural prior, the model can more effectively capture the dominant dependencies in the solution, enabling faster convergence and robust accuracy. Error distributions over all test instances (Figure 8) show that Variant TL has a median relative L^2 error 0.17%, similar to the median relative L^2 error 0.18% of the modified DeepONet. In test cases, Variant TL achieved better predictive accuracy in 64.90% of cases compared to the modified DeepONet. A non-parametric Wilcoxon two one-sided tests (TOST) for equivalence, with a margin of $\pm 0.02\%$, confirms that the two models are statistically equivalent in predictive accuracy, while a Spearman correlation coefficient $\rho = 0.769$ indicates strong agreement in error patterns.

Overall: Variant TL delivers predictive accuracy that is statistically equivalent to that of the modified DeepONet, while substantially reducing training time.

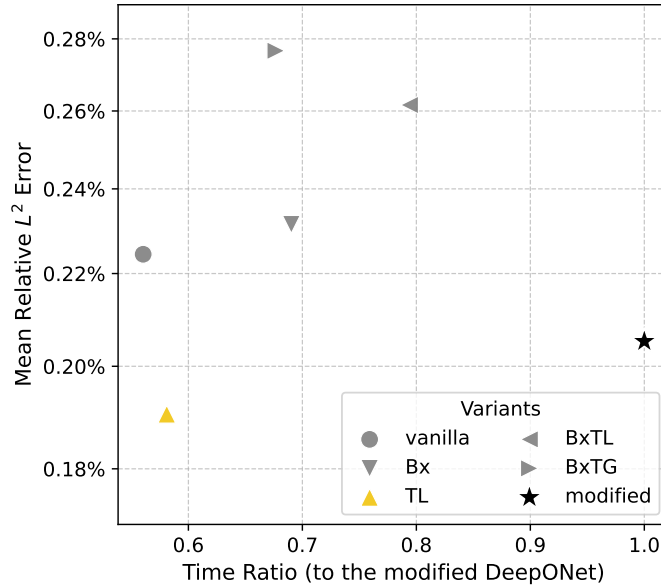


Figure 6: Performance comparison of model variants for the Diffusion–Reaction equation. The horizontal axis shows the average per-iteration training time ratio relative to the modified DeepONet, averaged over multiple random seeds (lower is faster), while the vertical axis shows the mean relative L^2 error (lower is better). Marker shapes distinguish different model variants; the modified DeepONet is shown in black, and the best-performing variant is highlighted in gold.

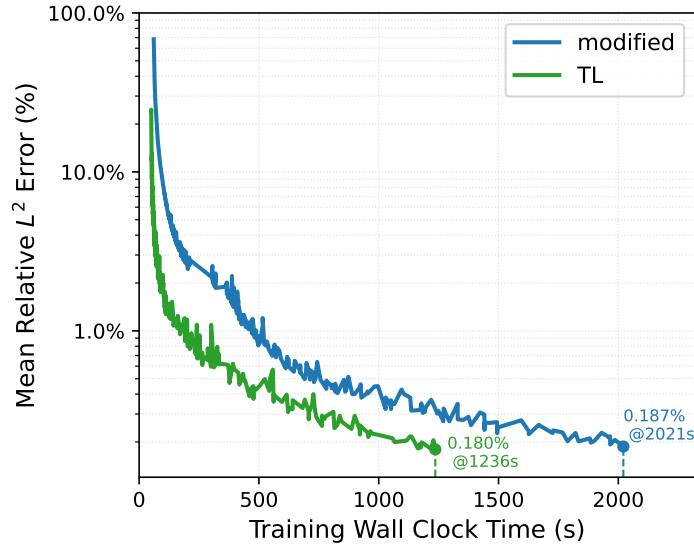


Figure 7: Comparison of training efficiency for the Diffusion–Reaction equation. The horizontal axis shows the wall-clock training time for a single representative run, and the vertical axis shows the mean relative L^2 error over all test cases (log scale). Dashed vertical lines and annotations mark the time at which each model completed 120,000 training iterations.

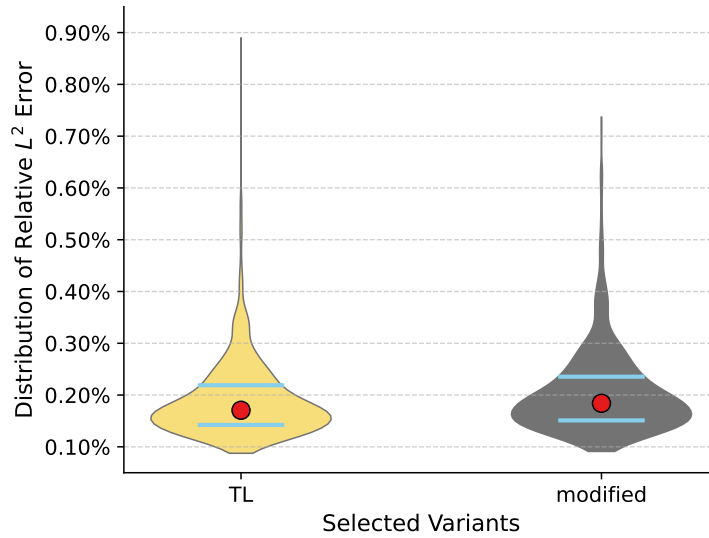


Figure 8: Distribution of relative L^2 errors for selected variants (gold: Variant TL; black: the modified DeepONet) on the Diffusion–Reaction equation, evaluated over multiple random seeds and test instances. Horizontal bars span the interquartile range (25th to 75th percentile), and red dots mark the median.

3.3 Burgers' Equation

We next consider the one-dimensional viscous Burgers' equation,

$$\frac{\partial s}{\partial t} + s \frac{\partial s}{\partial x} - \nu \frac{\partial^2 s}{\partial x^2} = 0, \quad (t, x) \in (0, 1] \times (0, 1), \quad (17)$$

subject to periodic boundary conditions

$$s(t, 0) = s(t, 1), \quad (18)$$

$$\frac{\partial s}{\partial x}(t, 0) = \frac{\partial s}{\partial x}(t, 1), \quad (19)$$

and the initial condition

$$s(0, x) = u(x), \quad x \in (0, 1). \quad (20)$$

We consider three viscosity values

$$\nu \in \{10^{-2}, 10^{-3}, 10^{-4}\}.$$

The initial conditions $u(x)$ are sampled from a Gaussian random field (GRF)

$$u \sim \mathcal{N}\left(0, 25^2(-\Delta + 5^2 I)^{-4}\right)$$

that satisfies the periodic boundary conditions. The learning objective is to approximate the solution operator G mapping the initial condition $u(x)$ to the corresponding spatiotemporal solution $s(t, x)$.

Variants comparison. Figures 9 to 11 compare the average per-iteration training time against the mean relative L^2 error for the Burgers' equation with viscosities $\nu = 10^{-2}$, 10^{-3} , and 10^{-4} , respectively. Across all three viscosities, the Transformer-inspired models shift markedly to the left of the modified DeepONet, indicating substantial reductions in per-iteration time cost. Again, this speedup can be attributed to the simpler network architectures of the variants. In terms of accuracy, the Variant TF remains close to the modified DeepONet at $\nu = 10^{-2}$ and $\nu = 10^{-3}$ (differences within a small margin), and becomes better at $\nu = 10^{-4}$. Overall, Variant TF offers a favorable speed–accuracy trade-off across viscosities: large gains in training speed while maintaining comparable accuracy in the moderate-/high-viscosity regimes and achieving a modest accuracy improvement in the low-viscosity regime. The Variant BxTF also achieves competitive predictive accuracy; at $\nu = 10^{-4}$, it attains the lowest mean relative L^2 error of approximately 12%, while also maintaining a fast per-iteration training speed. Both Variants TF and BxTF incorporate the leading Fourier coefficients of the initial condition into the trunk network, effectively introducing a low-pass filter that emphasizes the dominant low-frequency modes and discards high-frequency noise, conceptually similar to Fourier-based neural operator approaches [Zongyi Li et al. 2020]. In contrast, Variant BxTG embeds the entire initial condition into the trunk network, which often yields lower predictive accuracy

compared to Variants TF or BxTF. For Burgers' equation in the viscosity regimes considered here, the dynamics are primarily governed by the low-frequency Fourier modes of the initial condition, while high-frequency components are rapidly damped by viscosity (even at $\nu = 10^{-4}$, nonlinear energy transfer continues to favor lower modes) [Frisch and Bec 2001]. Including the full initial condition—containing high-frequency noise—may dilute the emphasis on these dynamically relevant structures, leading to reduced accuracy.

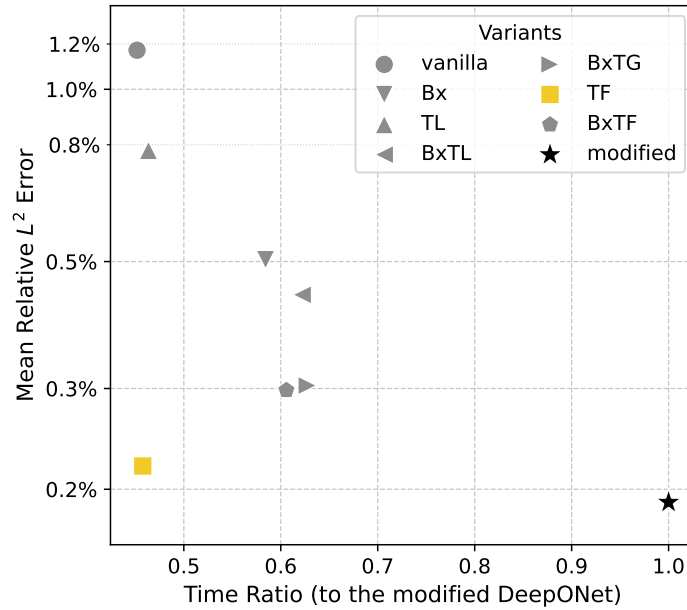


Figure 9: Performance comparison of model variants for the Burgers' equation ($\nu = 10^{-2}$). The horizontal axis shows the average per-iteration training time ratio relative to the modified DeepONet, averaged over multiple random seeds (lower is faster), while the vertical axis shows the mean relative L^2 error (lower is better). Marker shapes distinguish different model variants; the modified DeepONet is shown in black, and the best-performing variant is highlighted in gold.

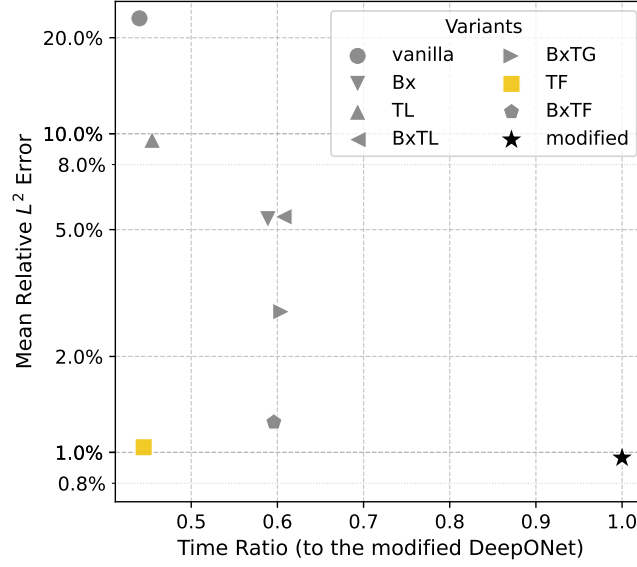


Figure 10: Performance comparison of model variants for the Burgers' equation ($\nu = 10^{-3}$). The horizontal axis shows the average per-iteration training time ratio relative to the modified DeepONet, averaged over multiple random seeds (lower is faster), while the vertical axis shows the mean relative L^2 error (lower is better). Marker shapes distinguish different model variants; the modified DeepONet is shown in black, and the best-performing variant is highlighted in gold.

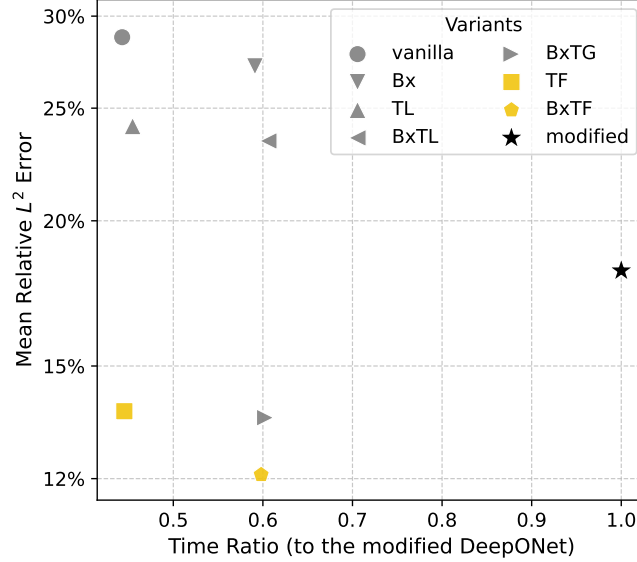


Figure 11: Performance comparison of model variants for the Burgers' equation ($\nu = 10^{-4}$). The horizontal axis shows the average per-iteration training time ratio relative to the modified DeepONet, averaged over multiple random seeds (lower is faster), while the vertical axis shows the mean relative L^2 error (lower is better). Marker shapes distinguish different model variants; the modified DeepONet is shown in black, and the best-performing variants are highlighted in gold.

Training efficiency. Figures 12 to 14 compare the convergence of the mean relative L^2 error with respect to wall-clock training time for selected variants at viscosities $\nu = 10^{-2}$, 10^{-3} , and 10^{-4} , respectively. Across all viscosities, the selected variants consistently reduce mean relative L^2 error more rapidly than the modified DeepONet, with all models trained for 200,000 iterations. At $\nu = 10^{-2}$, the Variant TF attains its final mean relative L^2 error of 0.208% in 3,041 s, whereas the modified DeepONet requires 5,643 s to reach the same accuracy (as indicated by the horizontal dotted line). At $\nu = 10^{-3}$, Variant TF achieves its final mean relative L^2 error of 0.981% in 2,569 s, compared to 5,387 s for the modified DeepONet to attain the same level. At $\nu = 10^{-4}$, Variant BxTF reaches a final mean relative L^2 error of 11.775% in 3,466 s, while the modified DeepONet converges more slowly to 17.337% in 5,812 s. These results underscore that Variants TF and BxTF deliver substantial reductions in training time while maintaining—and, in the low-viscosity regime, even improving—predictive accuracy.

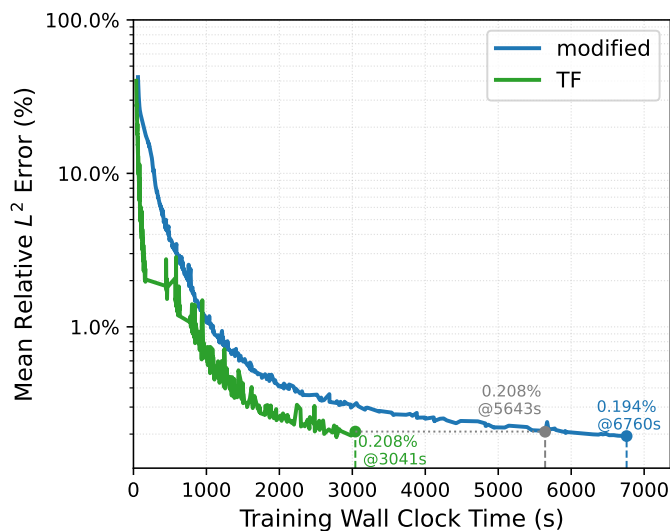


Figure 12: Comparison of training efficiency for the Burgers’ equation ($\nu = 10^{-2}$). The horizontal axis shows the wall-clock training time for a single representative run, and the vertical axis shows the mean relative L^2 error over all test cases (log scale). Dashed vertical lines and annotations mark the time at which each model completed training iterations. The dotted horizontal line indicates the wall-clock time at which the modified DeepONet reaches the same final accuracy as the TF variant.

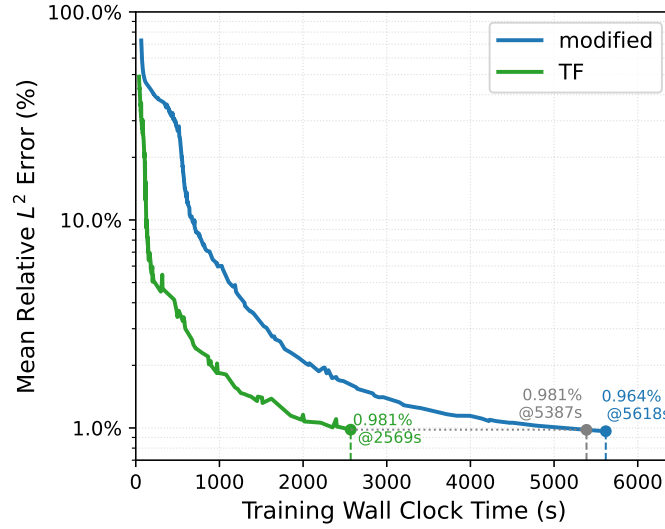


Figure 13: Comparison of training efficiency for the Burgers' equation ($\nu = 10^{-3}$). The horizontal axis shows the wall-clock training time for a single representative run, and the vertical axis shows the mean relative L^2 error over all test cases (log scale). Dashed vertical lines and annotations mark the time at which each model completed training iterations. The dotted horizontal line indicates the wall-clock time at which the modified DeepONet reaches the same final accuracy as the TF variant.

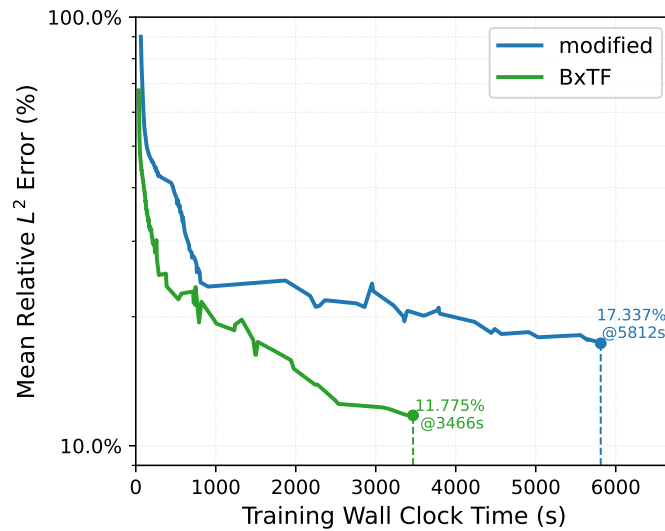


Figure 14: Comparison of training efficiency for the Burgers' equation ($\nu = 10^{-4}$). The horizontal axis shows the wall-clock training time for a single representative run, and the vertical axis shows the mean relative L^2 error over all test cases (log scale). Dashed vertical lines and annotations mark the time at which each model completed training iterations.

Error distribution and equivalence analysis. Figures 15 to 17 show the distributions of the relative L^2 error over all test instances for selected variants at viscosities $\nu = 10^{-2}$, 10^{-3} , and 10^{-4} , respectively. At $\nu = 10^{-2}$ (Figure 15), the Variant TF exhibits a median relative L^2 error slightly higher than that of the modified DeepONet. A non-parametric Wilcoxon two one-sided tests (TOST) (see Appendix C for the setup) rejects equivalence between Variant TF and the modified DeepONet with a margin of $\pm 0.01\%$ at this viscosity; the modified DeepONet achieves better accuracy, with a non-parametric Glass's $\Delta = 0.397$, corresponding to a small-to-moderate effect size. Thus, the accuracy compromise of Variant TF is modest, especially considering its substantially faster training speed. The Spearman correlation is strong ($\rho = 0.858$), indicating similar error patterns between Variant TF and the modified DeepONet. At $\nu = 10^{-3}$ (Figure 16), the Variant TF attains a median relative L^2 error comparable to that of the modified DeepONet. A non-parametric TOST for equivalence, with a margin of $\pm 0.06\%$, confirms that the two models are statistically equivalent in predictive accuracy, while the error patterns remain strongly correlated (Spearman $\rho = 0.869$). At $\nu = 10^{-4}$ (Figure 17), both Variants TF and BxTF achieve lower median relative L^2 errors than the modified DeepONet, with overall error distributions shifted downward relative to the modified DeepONet. In test cases, Variant BxTF achieved better predictive accuracy in 83.00% of cases compared to the modified DeepONet. The Wilcoxon TOST rejects equivalence in favor of the variants: Glass's $\Delta = -0.393$ for Variant TF and $\Delta = -0.568$ for Variant BxTF, indicating small-to-moderate improvements in predictive accuracy than the modified DeepONet (negative values indicate the modified DeepONet performs worse). The corresponding Spearman correlations are moderate to strong ($\rho = 0.515$ for TF vs. modified DeepONet, and $\rho = 0.542$ for BxTF vs. modified DeepONet), showing that their error variations remain partially aligned with those of the modified DeepONet across test cases.

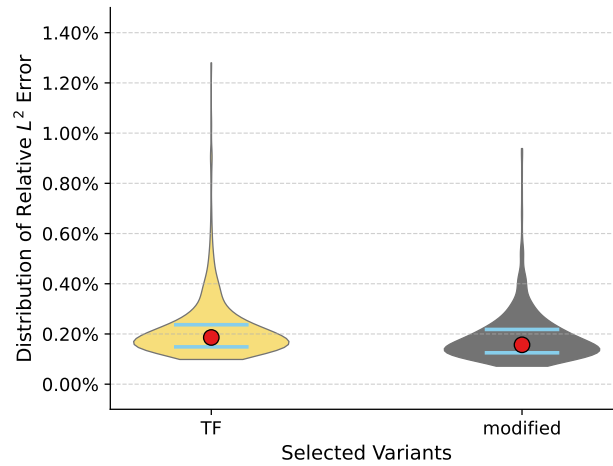


Figure 15: Distribution of relative L^2 errors for selected variants (gold: Variant TF; black: the modified DeepONet) on the Burgers' equation ($\nu = 10^{-2}$), evaluated over multiple random seeds and test instances. Horizontal bars span the interquartile range (25th to 75th percentile), and red dots mark the median.

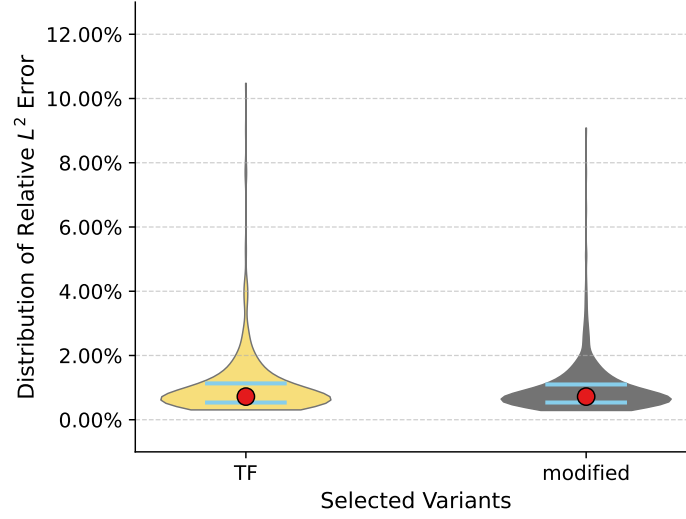


Figure 16: Distribution of relative L^2 errors for selected variants (gold: Variant TF; black: the modified DeepONet) on the Burgers' equation ($\nu = 10^{-3}$), evaluated over multiple random seeds and test instances. Horizontal bars span the interquartile range (25th to 75th percentile), and red dots mark the median.

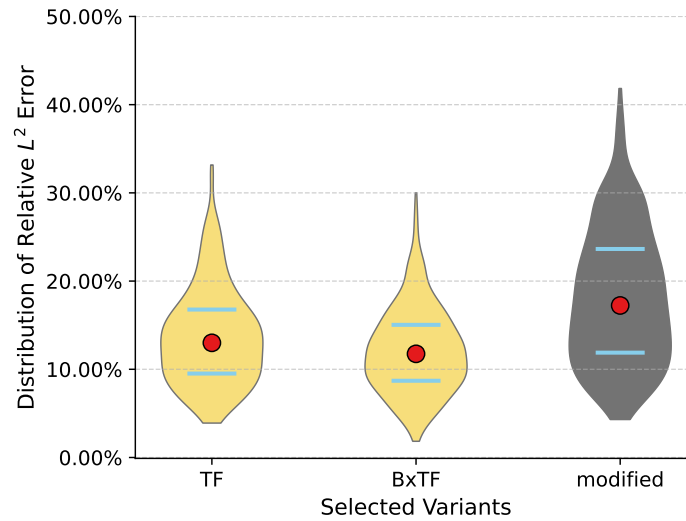


Figure 17: Distribution of relative L^2 errors for selected variants (gold: best-performing variants; black: the modified DeepONet) on the Burgers' equation ($\nu = 10^{-4}$), evaluated over multiple random seeds and test instances. Horizontal bars span the interquartile range (25th to 75th percentile), and red dots mark the median.

3.4 Korteweg–de Vries Equation

We finally consider the Korteweg–de Vries (KdV) equation,

$$\frac{\partial s}{\partial t} + s \frac{\partial s}{\partial x} + \delta^2 \frac{\partial^3 s}{\partial x^3} = 0, \quad (t, x) \in (0, 1) \times (0, 2\pi), \quad (21)$$

subject to periodic boundary conditions and the initial condition $s(0, x) = u(x)$. The initial conditions are parameterized as $u(x) = a \sin(x) + b \cos(x)$, where a and b are drawn from the standard normal distribution. Here, $\delta = 0.1$ denotes the dispersion coefficient. The learning objective is to approximate the solution operator G that maps the initial condition $u(x)$ to the corresponding spatiotemporal solution $s(t, x)$.

The performance of all evaluated models is summarized in Figures 18 to 20, with the modified DeepONet (black star marker in Figure 18) serving as the reference for both training time and accuracy. The KdV equation is particularly challenging to solve due to the possible presence of soliton solutions. Although in our current setting ($\delta = 0.1$ and low-frequency Fourier initial conditions) strong soliton interactions are less pronounced, the KdV equation in general is known to admit soliton solutions, making it challenging to solve accurately. Among the Transformer-inspired variants, Variant BxTG (gold marker in Figure 18) achieves the lowest mean relative L^2 error about 3.55% among the faster models, offering an average per-iteration speedup of about 60% while yielding slightly lower error than the 4.20% achieved by the modified DeepONet. The fast training speed of the Transformer-inspired variants is largely attributable to their simpler architectures. For the KdV equation, which is highly sensitive to initial conditions, feeding the full initial condition directly into the trunk network—as done in Variant BxTG—likely improves predictive accuracy. In contrast, in our setup, the initial conditions are only first-order Fourier modes, so feeding their coefficients alone (as in Variants TF and BxTF) may not provide sufficiently detailed information for optimal training. As an illustrative example, the convergence curves in Figure 19 show that Variant BxTG reaches a final mean relative L^2 error of 3.169% in 5,837 s, compared to 3.926% in 14,667 s for the modified DeepONet—representing a 60% reduction in wall-clock time, along with a lower final mean relative L^2 error. Moreover, at any given wall-clock time, the mean relative L^2 error of Variant BxTG (averaged over all test instances) remains consistently below that of the modified DeepONet, indicating faster convergence toward the optimum. Error distributions over all test instances (Figure 20) show that BxTG attains a similar median relative L^2 error to the modified DeepONet (0.45% and 0.44%, respectively), with comparable spread. From Figure 20, we observe that both error distributions are concentrated near small values, with low medians and 75th percentiles. However, a few large-error cases are present, with relative L^2 errors approaching 80%. These large errors for both models tend to occur in regions where the ground-truth solution exhibits steep gradients; see Appendix B for details. A non-parametric Wilcoxon two one-sided test (TOST) with an equivalence margin of $\pm 0.04\%$ concludes that Variant BxTG and the modified DeepONet are *not* equivalent in predictive accuracy: Variant BxTG has lower predictive error. The non-parametric Glass’s Δ is -0.054 , indicating that Variant BxTG is only a little bit better in accuracy than the modified DeepONet. In test

cases, Variant BxTG achieved better predictive accuracy in 56.00% of cases compared to the modified DeepONet. Furthermore, a Spearman correlation coefficient of $\rho = 0.860$ indicates a strong positive correlation in the error patterns of the two models.

Overall: Variant BxTG delivers measurably better predictive accuracy than the modified DeepONet for the KdV equation, while substantially reducing training time.

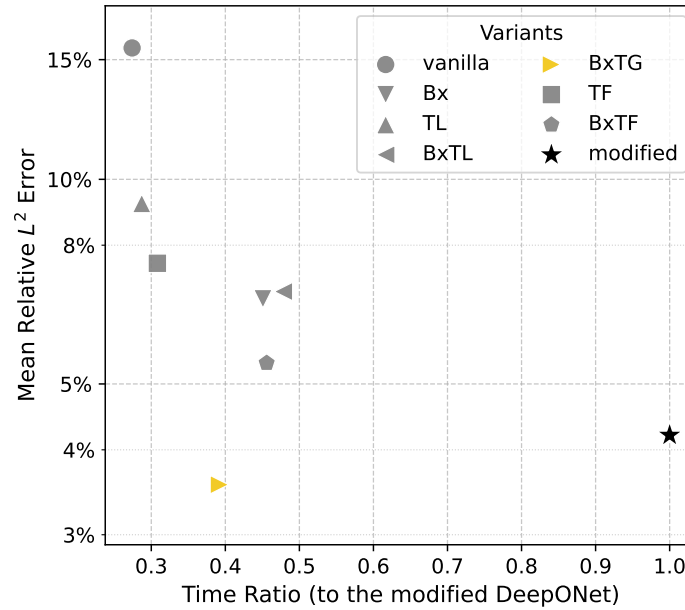


Figure 18: Performance comparison of model variants for the KdV equation. The horizontal axis shows the average per-iteration training time ratio relative to the modified DeepONet, averaged over multiple random seeds (lower is faster); the vertical axis shows the mean relative L^2 error (lower is better). Marker shapes distinguish different model variants; the modified DeepONet is shown in black, and the best-performing variant is highlighted in gold.

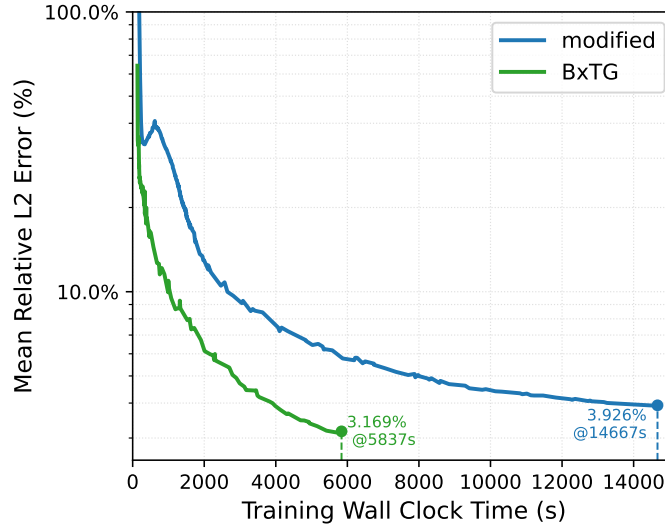


Figure 19: Comparison of training efficiency for the KdV equation. The horizontal axis shows the wall-clock training time for a single representative run, and the vertical axis shows the mean relative L^2 error over all test cases (log scale). Dashed vertical lines and annotations mark the reported final point for each run.

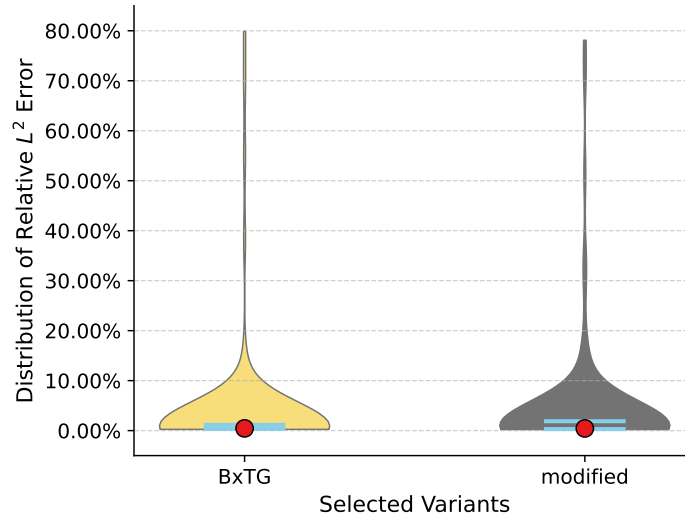


Figure 20: Distribution of relative L^2 errors for selected variants (gold: Variant BxTG; black: the modified DeepONet) on the KdV equation, evaluated over multiple random seeds and test instances. Horizontal bars span the interquartile range (25th to 75th percentile), and red dots mark the median.

4 Discussion and Conclusion

We proposed a series of *Transformer-inspired* variants of DeepONet that balance the trade-off between *predictive accuracy* and *computational efficiency* observed in the “vanilla” DeepONet and the modified DeepONet models. By injecting query-point information into the branch network and information of input function into the trunk network, our variants introduce *bidirectional cross-conditioning* between the branch and trunk networks, enabling dynamic dependencies while preserving the simplicity and efficiency of the “vanilla” DeepONet. These modifications are *structurally simple* and *non-intrusive*, requiring only minimal changes to the overall architecture.

Across the four PDE benchmarks, we observed that for each equation, there exists at least one variant that achieves accuracy comparable to (or better than) the modified DeepONet while offering improved training efficiency. Notably, the best-performing variant for each PDE appears to be closely related to the characteristics of the underlying equation. For example, in the case of Burgers’ equation, the most effective variant (TF) injects the leading Fourier coefficients of the initial condition into the trunk network. This design is theoretically motivated: the dynamics of the viscous Burgers’ equation are primarily governed by the low-frequency Fourier modes of the initial condition, while high-frequency components are rapidly damped due to viscosity. As a result, making the trunk network explicitly aware of the dominant Fourier modes helps it form more effective query-dependent representations, contributing to the improved predictive accuracy observed in Variant TF.

Looking ahead, one promising direction is to further refine the form of cross-conditioning between the input function and the trunk network. We experimented with injecting single-point evaluations of $u(x)$, the full function values, or a set of Fourier coefficients into the trunk. Inspired by the concept of the domain of dependence in PDEs, future work may explore supplying the trunk network with input-function information restricted to *a local neighborhood* of the query spatial point x . Such localized conditioning could yield better alignment with the underlying physics of the equation—particularly for hyperbolic PDEs—while preserving the training efficiency. This perspective may also serve as a bridge between classical numerical methods and neural operator design, offering a principled direction for unifying traditional numerical methods and neural operator design.

Code and Data Availability

To support reproducibility and facilitate future research, the code and all accompanying data will be made publicly available upon publication acceptance.

Acknowledgments

The work of Zhi-Feng Wei is supported by the U.S. Department of Energy (DOE) Office of Advanced Scientific Computing Research (ASCR) through the ASCR Distinguished

Computational Mathematics Postdoctoral Fellowship (Project No. 71268).

This project was completed with support from the U.S. Department of Energy, Advanced Scientific Computing Research program, under the Scalable, Efficient and Accelerated Causal Reasoning Operators, Graphs and Spikes for Earth and Embedded Systems (SEA-CROGS) project (Project No. 80278).

The computational work was performed using the Pacific Northwest National Laboratory (PNNL) Research Computing facilities.

PNNL is a multi-program national laboratory operated for the U.S. Department of Energy (DOE) by Battelle Memorial Institute under Contract No. DE-AC05-76RL01830.

A Data Generation and Network Parameters

In this appendix, we present the procedures and parameters used for data generation, neural network configuration, and implementation details, with the aim of facilitating the reproducibility of our results. To facilitate comparison with prior work, we adopt settings adapted from prior work: for the advection and Burgers’ equations we follow [S. Wang, H. Wang et al. 2022]; for the diffusion–reaction equation [S. Wang, H. Wang et al. 2021]; and for the KdV equation [Williams et al. 2024].

A.1 Data Generation

The datasets were generated, corresponding to the advection, diffusion–reaction, Burgers’, and Korteweg–de Vries (KdV) equations.

For the advection and diffusion–reaction equations, the spatially varying coefficient $u(x)$ —interpreted as the advection velocity in the advection equation and as the source term in the diffusion–reaction equation—was sampled from a Gaussian random field (GRF) with correlation length $l = 0.2$ and output scale 1.0. Reference solutions were computed on a uniform grid with $n_t = 101$ time steps and $n_x = 101$ spatial points. The advection equation was solved using the Lax–Wendroff finite-difference scheme [Iserles 2008]; the training set contains 1,000 functions and the test set contains 100 functions. The diffusion–reaction equation employed a second-order implicit finite difference method [Iserles 2008]; the training set contains 10,000 functions and the test set contains 1,000 functions.

Table A1: Data generation parameters for the Advection and Diffusion–Reaction equations.

Equation	Train size	Test size	Spatial domain	l	n_t	n_x
Advection	1,000	100	$[0, 1]$	0.2	101	101
Diffusion–Reaction	10,000	1,000	$[0, 1]$	0.2	101	101

The viscous Burgers’ equation is considered on the periodic domain $[0, 1]$ with viscosities $\nu = 10^{-2}$, 10^{-3} , and 10^{-4} . Initial conditions $u(x)$ for Burgers’ equation are sampled from a

Gaussian random field (GRF) as

$$u \sim \mathcal{N}\left(0, 25^2(-\Delta + 5^2 I)^{-4}\right).$$

The KdV equation is considered on the periodic domain $[0, 2\pi]$ with dispersion parameter $\delta = 0.1$. Initial conditions for the KdV equation are parameterized as $u(x) = a \sin x + b \cos x$, where a and b are independent standard normal random variables. For both the Burgers' and KdV equations, reference solutions are computed using a spectral Fourier discretization and a fourth-order stiff time-stepping scheme [Cox and Matthews 2002], with a spectral grid of $s = 4,096$ points and a time step of 10^{-4} . Solutions are stored on a coarse grid with n_t time levels and n_x spatial points, as listed in Table A2. For Burgers' equation, a total of 1,500 realizations are generated for each viscosity, with 1,000 used for training and 500 for testing. For the KdV equation, a total of 600 realizations are produced, with 500 used for training and 100 for testing.

Table A2: Data generation parameters for the Burgers' and KdV equations.

Equation	Train size	Test size	Domain	Spectral s	Δt	n_t	n_x
Burgers'	1,000	500	$[0, 1]$	4,096	10^{-4}	101	101
KdV	500	100	$[0, 2\pi]$	4,096	10^{-4}	101	129

A.2 Network Parameters

This subsection summarizes the hyperparameters used across all experiments. For clarity, we group them into three categories: (1) training setup in Table A3, (2) model specifications in Table A4, (3) sampling and loss weighting in Table A5.

Across all experiments we use the AdamW optimizer, `tanh` activations, and 64-bit precision. To address the challenge of loss balancing in physics-informed training, we employed both the conjugate kernel (CK) weighting strategy with moderate localization (see [Qadeer et al. 2023; S. Wang, H. Wang et al. 2022]) and the balanced-residual-decay-rate (BRDR) self-adaptive weighting scheme [W. Chen et al. 2025] in our numerical experiments. For each experiment, we report the results obtained from the weighting method that yielded better performance. All models are implemented and trained using the JAX framework (version 0.5.3), and optimized using Optax (version 0.2.4).

Fourier feature embeddings. For the diffusion–reaction equation, we use random Fourier features with 150 frequency draws; for each draw we include a paired sine–cosine term sharing the same random phase, yielding 300 features in total. For Burgers' equation viscosities 10^{-2} , 10^{-3} , and 10^{-4} , we use deterministic Fourier embeddings built from paired sine–cosine harmonics up to orders 4, 6, and 8, respectively (inclusive). For the KdV equation, we use a deterministic Fourier embedding with harmonics up to order 12 (inclusive). Therefore, for

Burgers’ and KdV equations, periodic boundary conditions are satisfied implicitly via the Fourier representation, so no explicit boundary sampling is required.

Table A3: Training setup.

Parameter	Advection	Diffusion–Reaction	Burgers’	KdV
Train size	1,000	10,000	1,000	500
Test size	100	1,000	500	100
Iterations	300,000	120,000	200,000	200,000
Batch size	10,000	10,000	10,000	16,384
Learning rate	0.001	0.001	0.001	0.001
LR schedule	Exp(500, 0.99) [†]	Exp(500, 0.99)	Exp(500, 0.99)	Exp(500, 0.99)
Optimizer	AdamW	AdamW	AdamW	AdamW
Activation	tanh	tanh	tanh	tanh
Precision (bits)	64	64	64	64

[†] Exponential decay with transition steps 500 and decay rate 0.99: $\eta_t = \eta_0 0.99^{t/500}$.

Table A4: Model specifications.

Parameter	Advection	Diffusion–Reaction	Burgers’	KdV
Branch width	100	50	100	128
Branch depth	6+1 [‡]	4+1	6+1	6+1
Trunk width	100	50	100	128
Trunk depth	6+1	4+1	6+1	6+1

[‡] “6 hidden +1” denotes 6 hidden layers plus an output layer.

Table A5: Sampling and loss weighting.

Parameter	Advection	Diffusion–Reaction	Burgers’	KdV
Initial allocation points	101	101	101	257
Boundary allocation points	101	101	NA*	NA*
Residual points	2,500	100	2,500	101 × 257
Weighting scheme	BRDR	CK	CK	CK

* boundary conditions are enforced implicitly by deterministic Fourier feature embeddings, so no explicit boundary sampling is required.

B Supporting Data and Extended Results

B.1 Raw Data Underlying Figures

We provide here the raw numerical data underlying Figures 3, 6, 9 to 11 and 18. To produce these plots, we compute the mean relative L^2 error over all test cases, averaged across all random seeds. In addition to the mean relative L^2 error, we also report the corresponding standard deviations, which are not reflected in the scatter plots such as Figure 18. The tables below also list the average training time per iteration (in seconds), which determines the values shown on the horizontal axes of scatter plots.

Table B1: Raw data for the Advection equation. Mean relative L^2 error and standard deviation (STD) are computed over all test cases and averaged across all random seeds. Average time per iteration and the ratio relative to the modified DeepONet are also reported.

Variant	Mean Rel. L^2 Error (%)	STD (%)	Avg. Time per Iter. (s)	Time Ratio
vanilla	2.096	0.569	0.0089	0.492
Bx	1.089	0.256	0.0097	0.534
TL	1.513	0.409	0.0092	0.508
BxTL	1.002	0.244	0.0100	0.552
BxTG	0.925	0.322	0.0101	0.559
modified	0.926	0.315	0.0181	1.000

Table B2: Raw data for the Diffusion–Reaction equation. Mean relative L^2 error and standard deviation (STD) are computed over all test cases and averaged across all random seeds. Average time per iteration and the ratio relative to the modified DeepONet are also reported.

Variant	Mean Rel. L^2 Error (%)	STD (%)	Avg. Time per Iter. (s)	Time Ratio
vanilla	0.224	0.097	0.0096	0.560
Bx	0.231	0.115	0.0118	0.690
TL	0.190	0.091	0.0099	0.581
BxTL	0.262	0.133	0.0136	0.794
BxTG	0.277	0.134	0.0116	0.677
modified	0.205	0.099	0.0171	1.000

Table B3: Raw data for the Burgers' equation with viscosity $\nu = 10^{-2}$. Mean relative L^2 error and standard deviation (STD) are computed over all test cases and averaged across all random seeds. Average time per iteration and the ratio relative to the modified DeepONet are also reported.

Variant	Mean Rel. L^2 Error (%)	STD (%)	Avg. Time per Iter. (s)	Time Ratio
vanilla	1.170	1.123	0.0140	0.452
Bx	0.504	0.358	0.0182	0.584
TL	0.782	0.571	0.0144	0.464
BxTL	0.437	0.329	0.0193	0.622
BxTG	0.304	0.187	0.0195	0.627
TF	0.220	0.137	0.0142	0.458
BxTF	0.298	0.181	0.0188	0.606
modified	0.190	0.116	0.0311	1.000

Table B4: Raw data for the Burgers' equation with viscosity $\nu = 10^{-3}$. Mean relative L^2 error and standard deviation (STD) are computed over all test cases and averaged across all random seeds. Average time per iteration and the ratio relative to the modified DeepONet are also reported.

Variant	Mean Rel. L^2 Error (%)	STD (%)	Avg. Time per Iter. (s)	Time Ratio
vanilla	23.012	14.192	0.0131	0.440
Bx	5.392	3.815	0.0176	0.589
TL	9.566	7.151	0.0136	0.455
BxTL	5.486	4.748	0.0181	0.607
BxTG	2.764	2.507	0.0181	0.604
TF	1.038	1.116	0.0133	0.445
BxTF	1.244	1.187	0.0178	0.596
modified	0.962	0.920	0.0299	1.000

Table B5: Raw data for the Burgers' equation with viscosity $\nu = 10^{-4}$. Mean relative L^2 error and standard deviation (STD) are computed over all test cases and averaged across all random seeds. Average time per iteration and the ratio relative to the modified DeepONet are also reported.

Variant	Mean Rel. L^2 Error (%)	STD (%)	Avg. Time per Iter. (s)	Time Ratio
vanilla	28.773	12.005	0.0133	0.443
Bx	27.163	10.892	0.0178	0.591
TL	24.128	8.487	0.0137	0.455
BxTL	23.427	11.986	0.0182	0.606
BxTG	13.541	6.654	0.0181	0.602
TF	13.715	6.805	0.0134	0.445
BxTF	12.094	6.060	0.0180	0.598
modified	18.119	10.371	0.0301	1.000

Table B6: Raw data for the KdV equation. Mean relative L^2 error and standard deviation (STD) are computed over all test cases and averaged across all random seeds. Average time per iteration and the ratio relative to the modified DeepONet are also reported.

Variant	Mean Rel. L^2 Error (%)	STD (%)	Avg. Time per Iter. (s)	Time Ratio
vanilla	15.606	17.957	0.0223	0.274
Bx	6.671	16.192	0.0367	0.451
TL	9.216	15.194	0.0234	0.287
BxTL	6.837	16.372	0.0389	0.478
BxTG	3.554	12.292	0.0319	0.392
TF	7.525	17.463	0.0251	0.308
BxTF	5.367	14.556	0.0371	0.456
modified	4.203	12.405	0.0814	1.000

The raw numerical data underlying Figures 19 and 20 and other similar figures (e.g., additional efficiency-accuracy curves and full per-instance error distributions) involve extensive time series and individual error records, and are therefore omitted here for brevity. For violin plots, we report in Table B7 the median and interquartile range (Q1, Q3) of the relative L^2 error. The full datasets are available from the authors upon request.

Table B7: Summary statistics (Q1, Median, Q3) of the relative L^2 error for selected variants in violin plots. All values are reported in percent.

Equation	Variant	Q1 (%)	Median (%)	Q3 (%)
Advection	BxTG	0.68	0.85	1.08
	modified	0.67	0.88	1.10
Diffusion–Reaction	TL	0.14	0.17	0.22
	modified	0.15	0.18	0.24
Burgers' ($\nu = 10^{-2}$)	TF	0.15	0.19	0.24
	modified	0.13	0.16	0.22
Burgers' ($\nu = 10^{-3}$)	TF	0.54	0.72	1.13
	modified	0.54	0.72	1.10
Burgers' ($\nu = 10^{-4}$)	TF	9.52	13.00	16.77
	BxTF	8.70	11.75	15.04
	modified	11.89	17.2300	23.64
KdV	BxTG	0.35	0.45	1.16
	modified	0.31	0.44	1.87

B.2 Reference-Prediction Comparisons and Discussion

In this section, we visualize representative cases by comparing the reference solution with predictions from selected model variants. For each PDE, we report the modified DeepONet and a top-performing Transformer-inspired variant; each panel shows the reference solution, the model prediction, and the pointwise absolute error.

For the Advection equation, we compare the modified DeepONet with the BxTG variant; see Figures B1 and B2. On the shown instance, the two models achieve comparable accuracy (relative L^2 errors 0.87% for the modified DeepONet and 0.91% for the Variant BxTG).

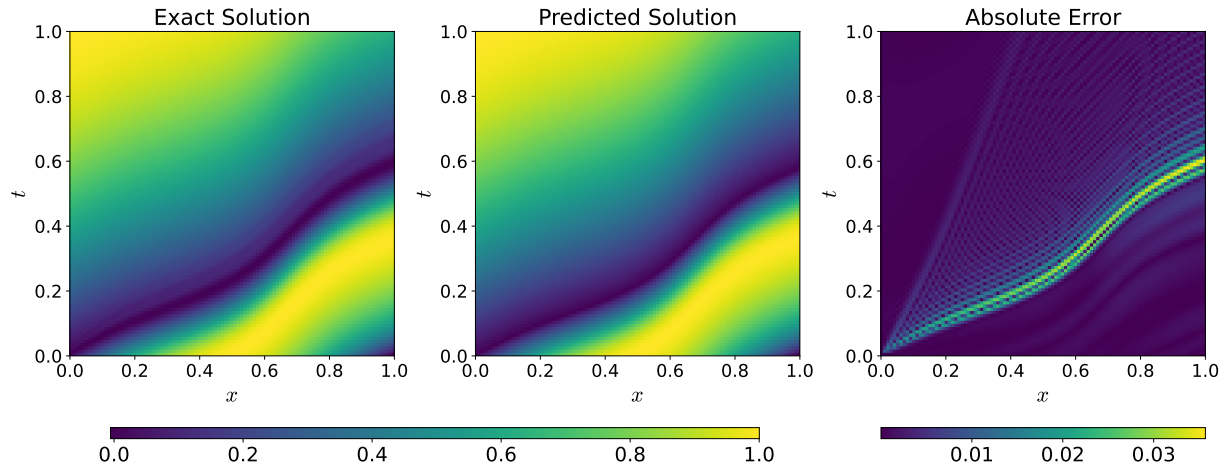


Figure B1: Advection (the modified DeepONet). Left to right: reference solution, model prediction, and absolute error on a representative training instance. The L^2 relative error is 0.87%.

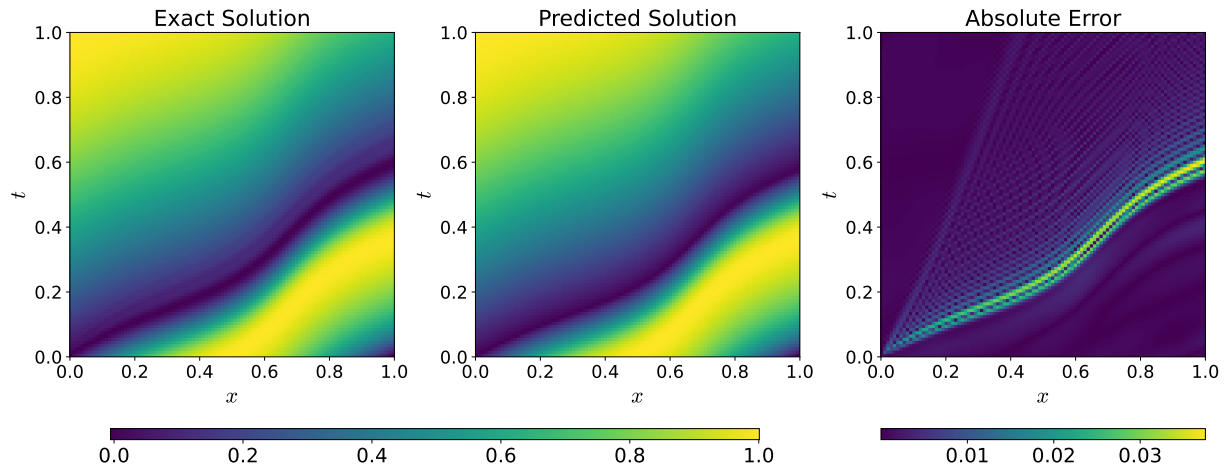


Figure B2: Advection (Variant BxTG). Left to right: reference solution, model prediction, and absolute error on the same instance as in Figure B1. The L^2 relative error is 0.91%.

For the Diffusion–Reaction equation, we compare the modified DeepONet with the TL variant; see Figures B3 and B4. The two models again attain comparable accuracy (relative L^2 errors 0.14% for the modified DeepONet and 0.15% for the Variant TL).

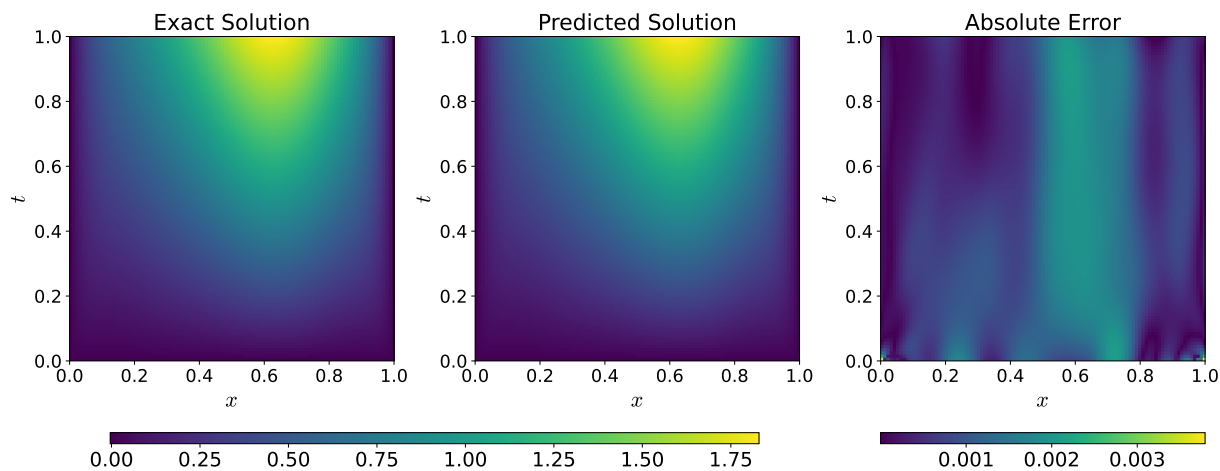


Figure B3: Diffusion–Reaction (the modified DeepONet). Left to right: reference solution, model prediction, and absolute error on a representative training instance. The L^2 relative error is 0.14%.

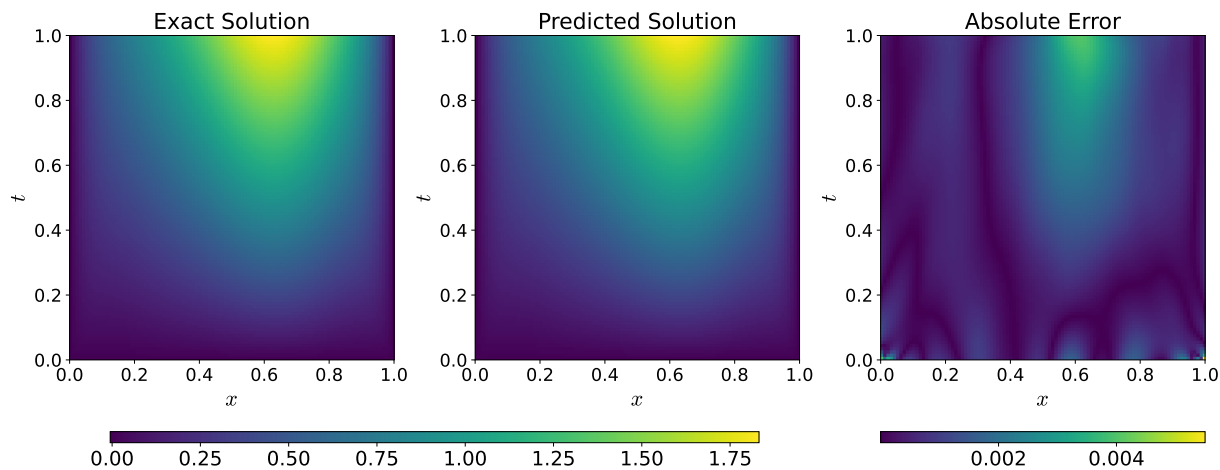


Figure B4: Diffusion–Reaction (Variant TL). Left to right: reference solution, model prediction, and absolute error on the same instance as in Figure B3. The L^2 relative error is 0.15%.

For Burgers' equation with viscosity 10^{-2} , we compare the modified DeepONet with Variant TF; see Figures B5 and B6. The two methods perform similarly on this instance (relative L^2 errors 0.19% for the modified DeepONet and 0.17% for the variant TF).

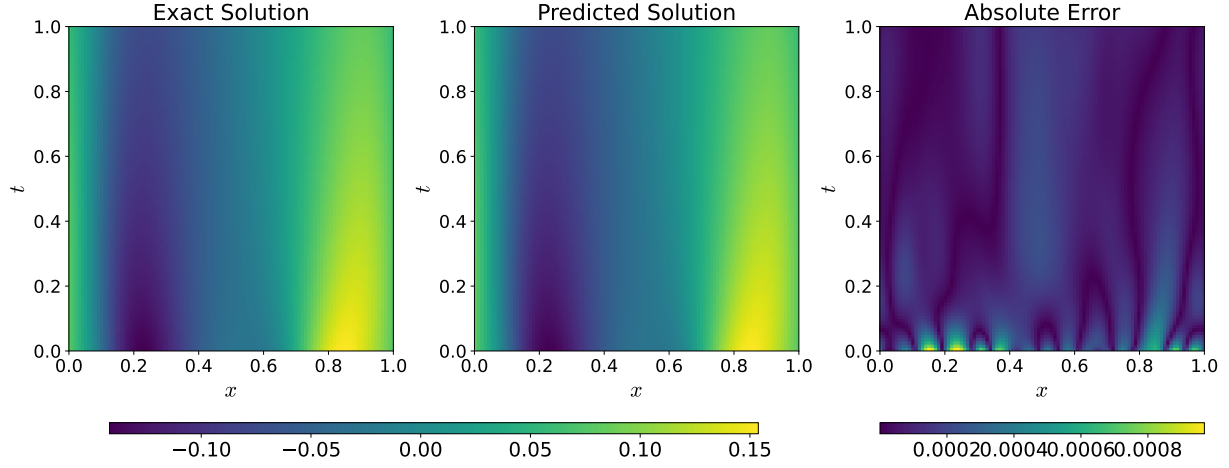


Figure B5: Burgers' equation with viscosity 10^{-2} (the modified DeepONet). Left to right: reference solution, model prediction, and absolute error on a representative training instance. The L^2 relative error is 0.19%.

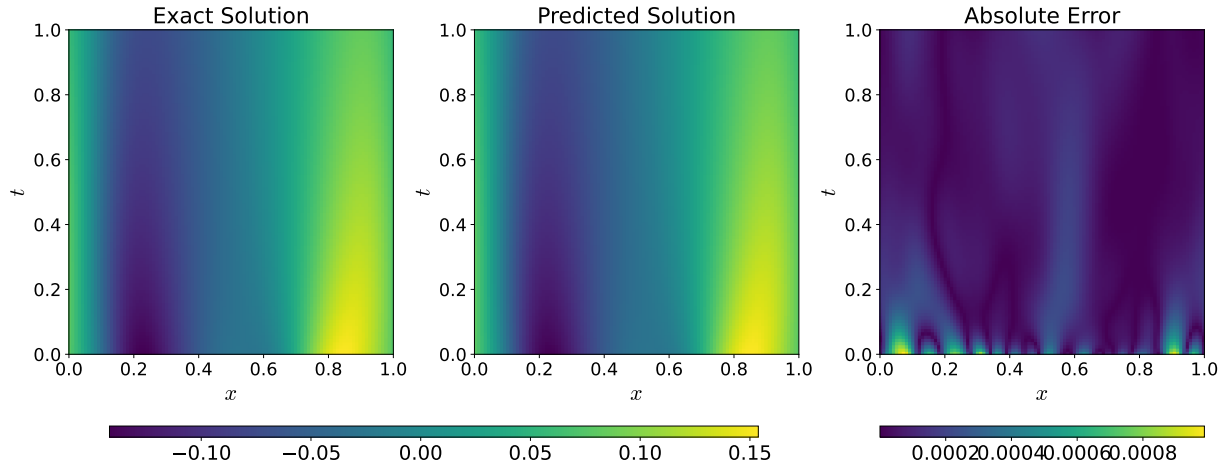


Figure B6: Burgers' equation with viscosity 10^{-2} (Variant TF). Left to right: reference solution, model prediction, and absolute error on the same instance as in Figure B5. The L^2 relative error is 0.17%.

For Burgers' equation with viscosity 10^{-3} , we again compare the modified DeepONet with Variant TF; see Figures B7 and B8. Variant TF achieves a slightly lower error (0.43%) than the modified DeepONet (0.61%) on the shown instance.

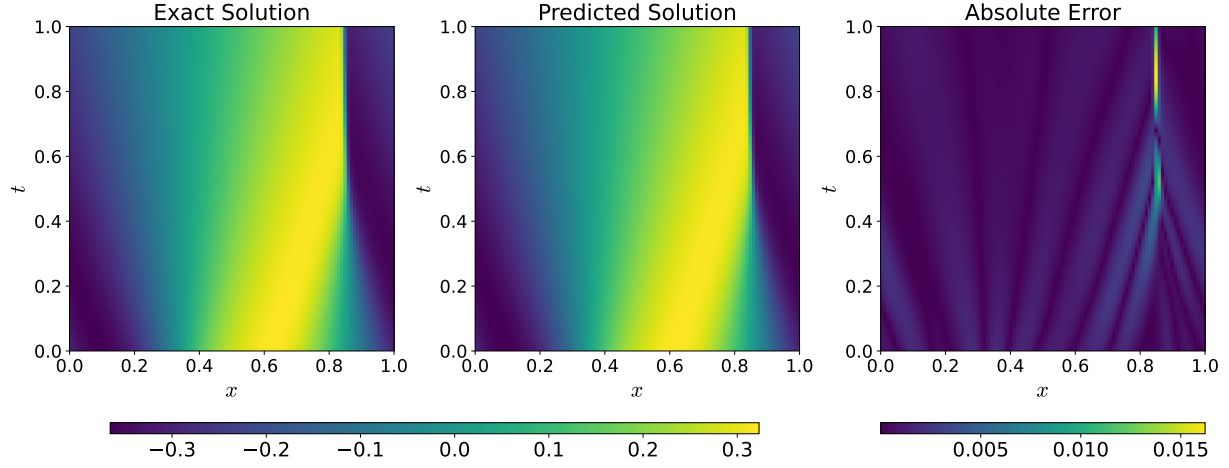


Figure B7: Burgers' equation with viscosity 10^{-3} (the modified DeepONet). Left to right: reference solution, model prediction, and absolute error on a representative training instance. The L^2 relative error is 0.61%.

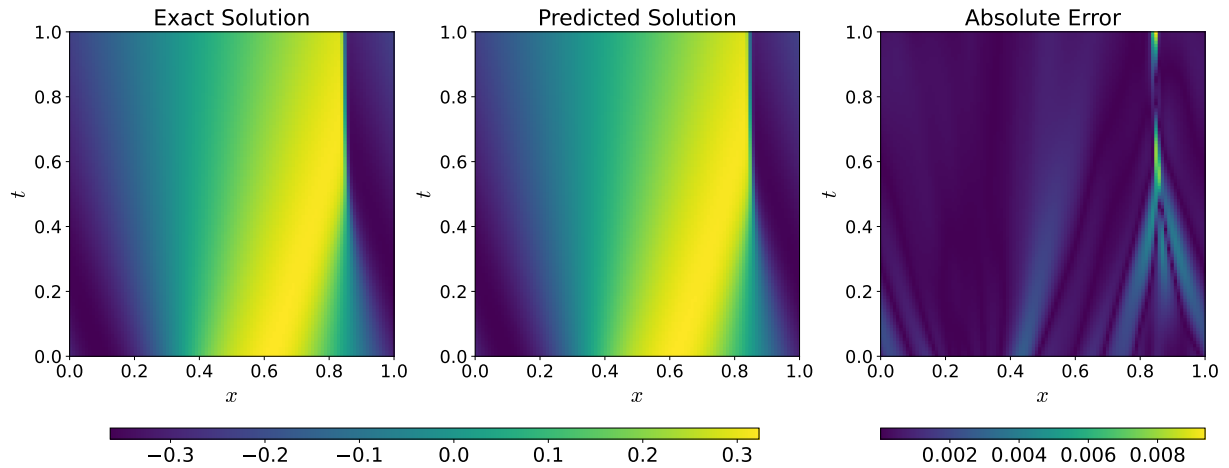


Figure B8: Burgers' equation with viscosity 10^{-3} (Variant TF). Left to right: reference solution, model prediction, and absolute error on the same instance as in Figure B7. The L^2 relative error is 0.43%.

For Burgers' equation with viscosity 10^{-4} , we compare the modified DeepONet with Variants TF and BxTF; see Figures B9 to B11. Both Transformer-inspired variants outperform the modified DeepONet on this instance (relative L^2 errors 25.21% for the modified DeepONet, 13.10% for TF, and 15.16% for BxTF).

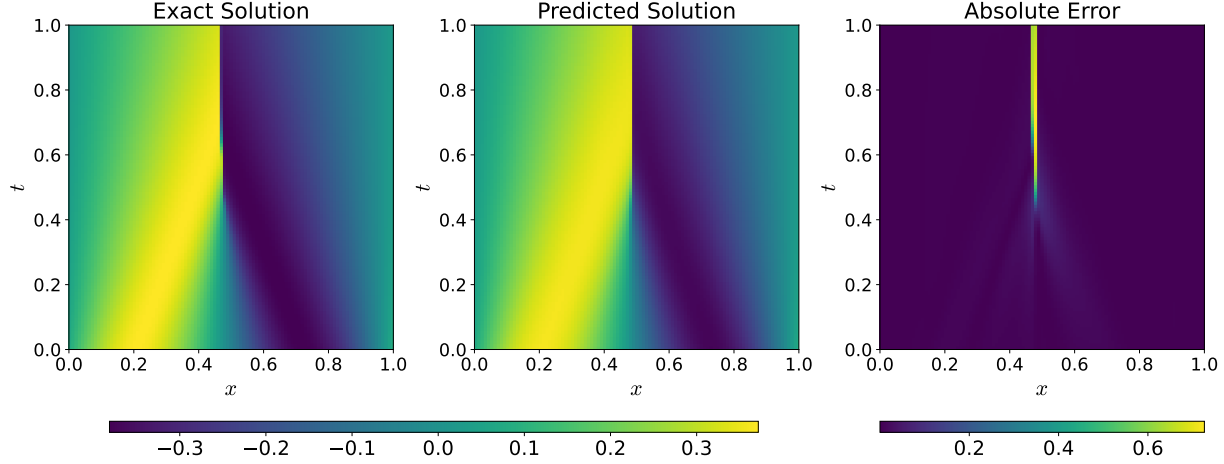


Figure B9: Burgers' equation with viscosity 10^{-4} (modified DeepONet). Left to right: reference solution, model prediction, and absolute error on a representative training instance. The L^2 relative error is 25.21%.

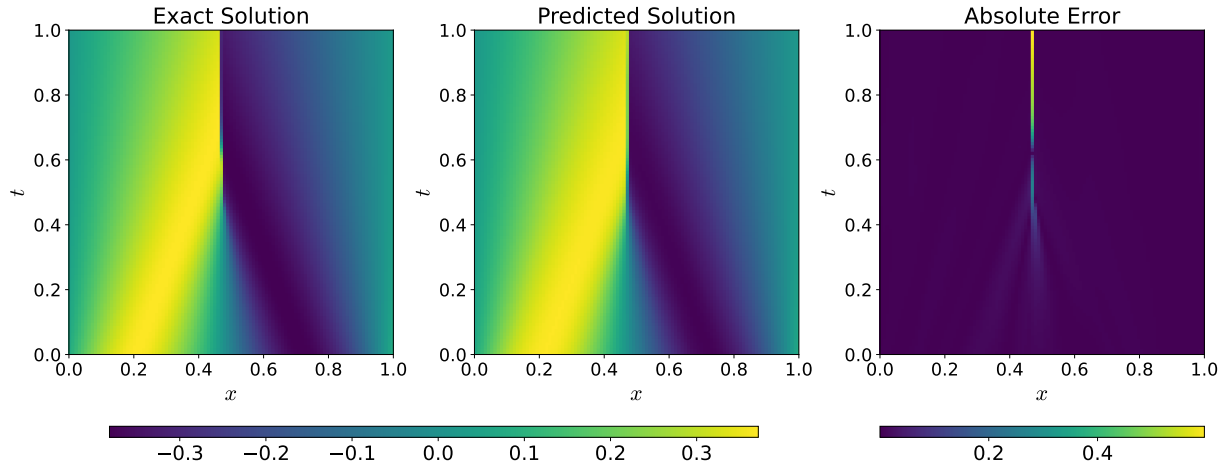


Figure B10: Burgers' equation with viscosity 10^{-4} (Variant TF). Left to right: reference solution, model prediction, and absolute error on the same instance as in Figure B9. The L^2 relative error is 13.10%.

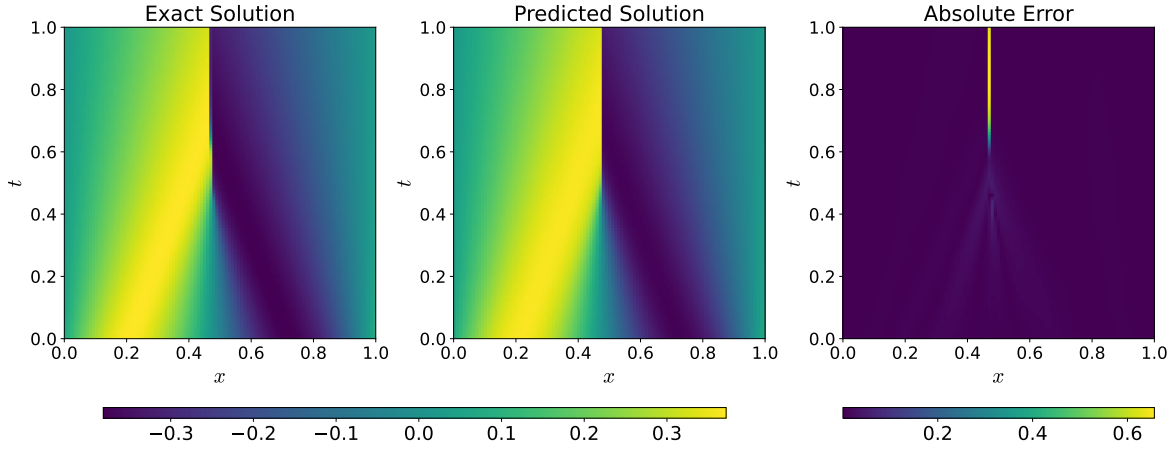


Figure B11: Burgers' equation with viscosity 10^{-4} (Variant BxTF). Left to right: reference solution, model prediction, and absolute error on the same instance as in Figure B9. The L^2 relative error is 15.16%.

For the KdV equation, we compare the modified DeepONet with the BxTG variant. Figures B12 and B13 shows a representative test case of moderate difficulty on which both models achieve comparable accuracy. In addition, as suggested by the violin plot in Figure 20, a small number of test cases exhibit relatively large errors. Closer inspection reveals that the errors are highly localized in regions of space-time where the exact solution exhibits large gradients; see Figures B14 and B15. On this challenging instance, Variant BxTG attains lower error (i.e., better accuracy) than the modified DeepONet.

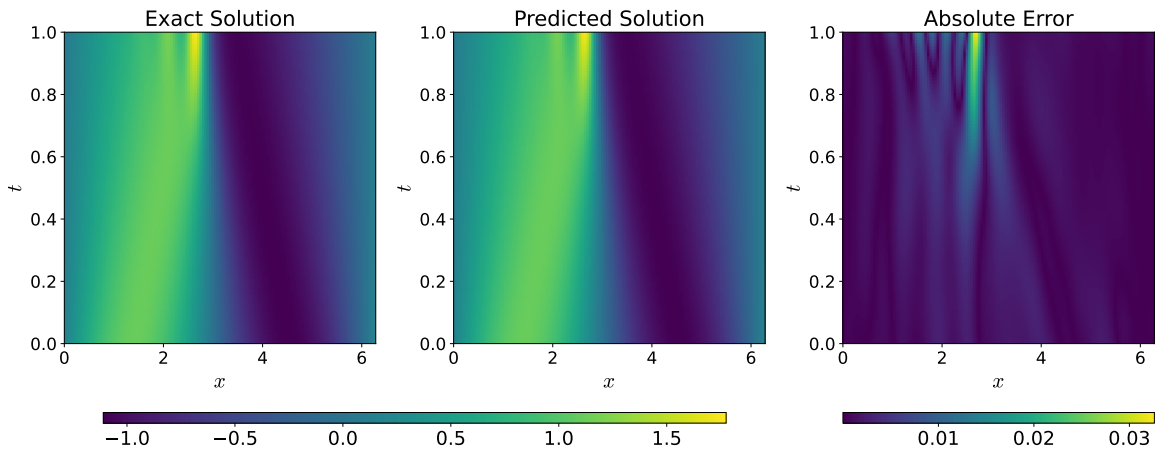


Figure B12: KdV equation (the modified DeepONet). Left to right: reference solution, model prediction, and absolute error on a representative training instance. The L^2 relative error is 0.44%.

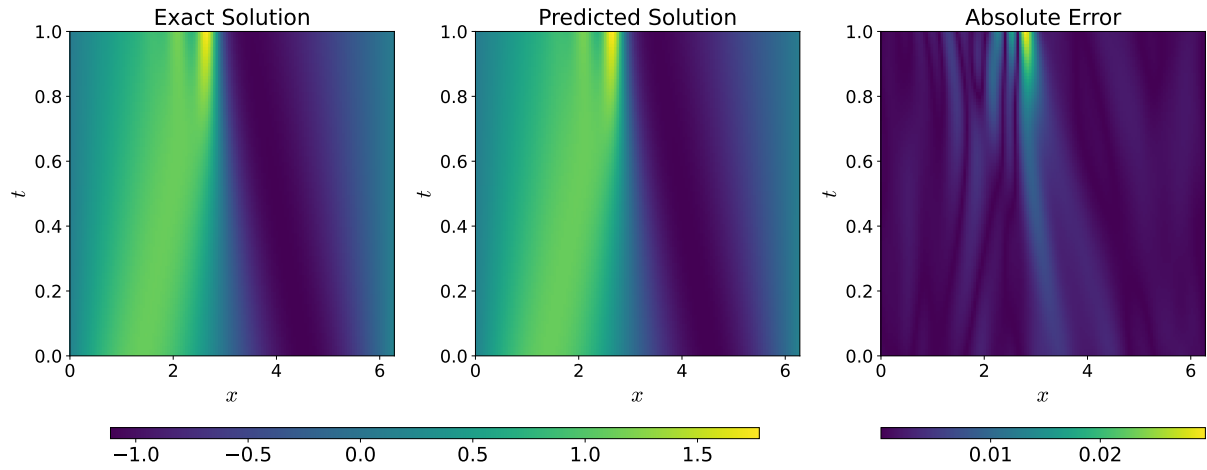


Figure B13: KdV equation (Variant BxTG). Left to right: reference solution, model prediction, and absolute error on a representative training instance. The L^2 relative error is 0.41%.

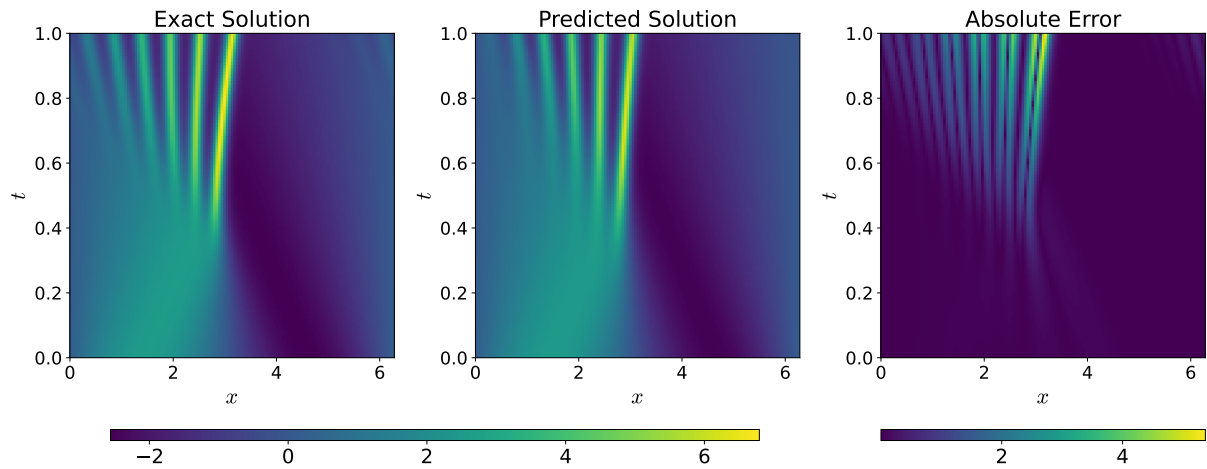


Figure B14: KdV equation (the modified DeepONet). Left to right: reference solution, model prediction, and absolute error on a representative training instance. The L^2 relative error is 37.96%.

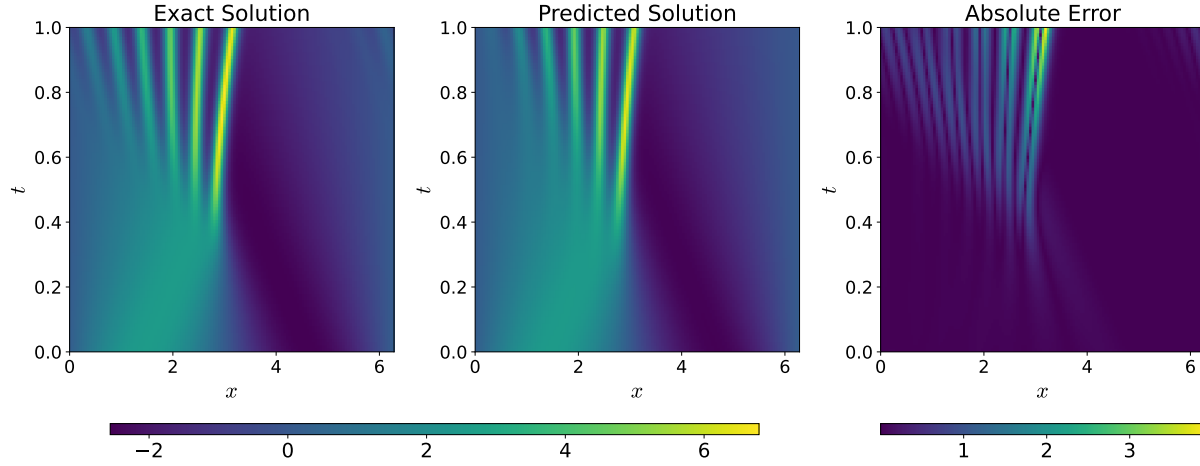


Figure B15: KdV equation (Variant BxTG). Left to right: reference solution, model prediction, and absolute error on a representative training instance. The L^2 relative error is 24.31%.

B.3 Results Reported in the Literature

In this section, we list selected results from related literature for reference and contextual comparison.

The advection equation was studied in [S. Wang, H. Wang et al. 2022] using a physics-informed modified DeepONet. A mean L^2 relative error of 0.95% with a standard deviation of 0.23% was reported, achieved through moderate local neural tangent kernel (NTK) methods for loss term balancing. The input function distribution used in their work is the same as in our study.

In [S. Wang, H. Wang et al. 2021], the authors studied a diffusion–reaction equation using a physics-informed “vanilla” DeepONet. Fixed weights were employed for loss term balancing, and a mean L^2 relative error of 0.45% with a standard deviation of 0.16% was reported. The input function distribution remains the same as in our study. Improved performance in our results is attributed to the use of random Fourier feature embedding.

In [S. Wang, H. Wang et al. 2022], Burgers’ equation was studied under viscosities of 10^{-2} , 10^{-3} , and 10^{-4} . The reported mean L^2 relative errors (with standard deviations) were $1.03\% \pm 1.35\%$, $3.69\% \pm 3.63\%$, and $7.95\% \pm 5.29\%$, respectively. For viscosities 10^{-2} and 10^{-3} , our method achieved better accuracy, which we attribute to the use of deterministic Fourier feature embedding.

In [Williams et al. 2024], transfer learning techniques were applied to the study of both Burgers’ and KdV equations using a physics-informed modified DeepONet. For the viscous Burgers’ equation with viscosity 10^{-4} , the network was initialized with pretrained parameters from the case with viscosity 10^{-3} . This approach yielded a mean L^2 relative error of 7.03% with a standard deviation of 4.94%, with moderate local NTK adaptive weights used for loss

term balancing. The initial condition distribution used for the Burgers' equation matches that of our study.

For the KdV equation, the model was initialized with parameters transferred from the Burgers' equation with viscosity 10^{-4} , which itself had been transfer-initialized from viscosity 10^{-3} . A mean L^2 relative error of 3.29% with standard deviation 5.94% was reported, using local CK adaptive weights for balancing the loss terms. The higher error can be attributed to the increased difficulty of their initial conditions than ours.

C Rigorous Statistical Analysis Procedures

In this appendix, we detail the rigorous statistical analysis procedures used for a comparative evaluation of our top-performing model variants and the baseline modified DeepONet model. Recognizing that our readership may have diverse backgrounds, we have included a concise summary of the fundamental statistical theories and principles that inform our analysis, aiming to make the content self-contained and accessible.

For a given equation, we denote the sequences of L^2 relative errors for the top-performing model variant and the baseline modified DeepONet model as

$$\{\varepsilon_i^{(v)}\}_{i=1}^N$$

and

$$\{\varepsilon_i^{(b)}\}_{i=1}^N,$$

respectively. Their element-wise difference sequence is

$$\{d_i\}_{i=1}^N := \{\varepsilon_i^{(v)} - \varepsilon_i^{(b)}\}_{i=1}^N.$$

C.1 Percentage of Negative Difference

We first examine the element-wise difference sequence. Each negative term in the sequence $\{d_i\}_{i=1}^N$ indicates a test case where the variant model outperformed the baseline. Thus, the percentage of negative terms serves as a direct metric for the frequency of the variant's better accuracy across the test dataset.

C.2 Wilcoxon Two One-Sided Tests (TOST) for Equivalence

To formally test for statistical equivalence in accuracy between the variant model and the baseline model, we employ the Wilcoxon two one-sided tests (TOST) procedure [Wilcoxon 1945]. This non-parametric approach assesses whether the error distributions of the variant and baseline models are effectively the same. The test is performed on the element-wise difference sequence $\{d_i\}_{i=1}^N$.

C.2.1 Lower-Bound Test

The lower-bound test determines whether the theoretical median, M_d , of the underlying theoretical distribution of differences $\{d_i\}_{i=1}^N$ is greater than a predefined equivalence margin, $-\Delta$. The null (H_0) and alternative (H_1) hypotheses for this test are formulated as:

$$\begin{aligned} H_0: M_d &\leq -\Delta, \\ H_1: M_d &> -\Delta. \end{aligned}$$

The test statistic is based on the ranks of the absolute values of the differences, $\{d_i\}_{i=1}^N$. First, we establish an unsigned rank sequence, $\{\hat{R}_i\}_{i=1}^N$, where the rank $\hat{R}_i = 1$ is assigned to the difference with the smallest absolute value, and $\hat{R}_i = N$ is assigned to the one with the largest absolute value.

Next, we construct the signed-rank sequence $\{R_i\}_{i=1}^N$. A sign is assigned to each unsigned rank \hat{R}_i based on its corresponding difference d_i : if $d_i > -\Delta$, we set $R_i = +\hat{R}_i$; otherwise, we set $R_i = -\hat{R}_i$. From this sequence, we define the positive and negative rank-sum statistics as:

$$w^+ := \sum_{R_i > 0} R_i \quad \text{and} \quad w^- := \sum_{R_i \leq 0} R_i.$$

The objective is to calculate the p -value, $p^{(\text{lower})}$, defined as the probability of observing a positive (stochastic) rank-sum statistic W^+ at least as large as the measured w^+ , under the assumption that the null hypothesis H_0 is true. Calculating this probability directly under the composite hypothesis H_0 (i.e., $M_d \leq -\Delta$) is complex. We therefore simplify the problem by first analyzing the boundary case of the null hypothesis, $\widetilde{H}_0: M_d = -\Delta$. Under this simpler condition, we calculate a corresponding probability, $\widetilde{p}^{(\text{lower})}$. This approach, however, hinges on understanding the stochastic nature of W^+ , whose source of randomness has not yet been defined. We will first clarify this, and then demonstrate that $\widetilde{p}^{(\text{lower})}$ provides a valid p -value for the original hypothesis test.

The source of randomness for the test statistic W^+ arises from the assumption of symmetry inherent in the null hypothesis. Specifically, under the boundary condition \widetilde{H}_0 (where the median $M_d = -\Delta$), any difference d_i is equally likely to fall above or below $-\Delta$. Consequently, when constructing the signed-rank sequence $\{R_i\}_{i=1}^N$, the assignment of a positive or negative sign to each corresponding unsigned rank \hat{R}_i is an equiprobable event. This generates a sample space of 2^N possible, equally likely signed-rank sequences. The random variable W^+ is thus defined as the positive rank-sum calculated over this discrete uniform probability space.

We now connect the probability calculated in the boundary case, $\widetilde{p}^{(\text{lower})}$, to the p -value for the original composite hypothesis, $p^{(\text{lower})}$. The boundary case \widetilde{H}_0 represents the “edge” of the parameter space defined by H_0 . For any other case within H_0 (i.e., where $M_d < -\Delta$), the distribution of $\{d_i\}_{i=1}^N$ is shifted further to the left. This implies that the probability of observing a difference greater than $-\Delta$ is lower than it is under the boundary condition. Consequently, the probability of achieving a given positive rank-sum w^+ is maximized under \widetilde{H}_0 . This gives us the following inequality:

$$\sup_{M_d \leq -\Delta} \mathbf{P}[W^+ \geq w^+] = \mathbf{P}_{\widetilde{H}_0}[W^+ \geq w^+].$$

By definition, the p -value is the maximum probability of observing a result at least as extreme as the one measured, over the entire parameter space of the null hypothesis. Based on the reasoning above, this maximum occurs at the boundary. Therefore, we can calculate the p -value for the composite hypothesis H_0 by using the simpler boundary case \widetilde{H}_0 :

$$p^{(\text{lower})} := \sup_{M_d \leq -\Delta} \mathbf{P} [W^+ \geq w^+] = \mathbf{P}_{\widetilde{H}_0} [W^+ \geq w^+] = \widetilde{p}^{(\text{lower})}.$$

A small $p^{(\text{lower})}$ indicates that the observed data is unlikely if the null hypothesis were true. Following standard statistical convention, if $p^{(\text{lower})}$ is below a pre-specified significance level (e.g., 0.05), we reject H_0 and adopt the alternative hypothesis, H_1 .

C.2.2 Upper-Bound Test

Symmetrically, the upper-bound test determines whether the theoretical median of the underlying theoretical distribution of differences, M_d , is less than a predefined equivalence margin, $+\Delta$. The null (H_0) and alternative (H_1) hypotheses are formulated as:

$$\begin{aligned} H_0: M_d &\geq +\Delta, \\ H_1: M_d &< +\Delta. \end{aligned}$$

The corresponding p -value, $p^{(\text{upper})}$, is derived using a procedure analogous to that of the lower-bound test, but by testing against the upper margin.

C.2.3 Conclusion for Equivalence

The two one-sided tests are combined to reach a conclusion on equivalence. If both the lower-bound and upper-bound tests are statistically significant (i.e., $p^{(\text{lower})} < 0.05$ and $p^{(\text{upper})} < 0.05$), we reject both corresponding null hypotheses. This allows us to conclude that the theoretical median of the difference distribution, M_d , lies within the equivalence interval $(-\Delta, +\Delta)$. In practical terms, this outcome provides statistical evidence that the variant and baseline models are equivalent in prediction accuracy as reflected by their L^2 relative errors.

In practice, determining an appropriate equivalence margin Δ is context-dependent and often requires a balance between statistical rigor and practical interpretability (cf. [Schuirmann 1987](#); [Wellek 2010](#)). In analogy to the use of relative thresholds in equivalence testing (e.g., the 20% rule in bioequivalence studies), we set the equivalence margin as one fifth of the minimal error over all test cases given by the baseline model, i.e.,

$$\Delta := 0.2 \times \min_i \varepsilon_i^{(\text{b})}.$$

This choice ensures that the equivalence margin is (1) anchored to the performance scale of the baseline, (2) interpretable as a practically negligible difference, and (3) objectively determined from the data rather than set arbitrarily and subjectively.

C.3 Determining the Model with Better Accuracy if Inequivalent

If the TOST procedure does not establish equivalence, we proceed to determine which model exhibits better accuracy. In this scenario, the theoretical median of the underlying theoretical distribution of the differences, M_d , is presumed to lie outside the equivalence interval $(-\Delta, +\Delta)$. We use the sample median of the observed differences, denoted \widehat{M}_d , as an estimator for the theoretical median. The sign of the sample median indicates better model:

- If $\widehat{M}_d > 0$, the differences tend to be positive, suggesting that the baseline model has lower prediction errors and thus better accuracy.
- If $\widehat{M}_d < 0$, the differences tend to be negative, suggesting that the variant model has lower prediction errors and therefore outperforms the baseline in prediction accuracy.

C.4 Quantifying the Accuracy Difference

If the models are found to be inequivalent, we next quantify the magnitude of the difference of errors. For this purpose, we employ a non-parametric effect size measure analogous to Glass's Δ [Glass 1976; Wilcox 2011]. This metric standardizes the difference of errors by scaling it against the variability of the baseline model.

The numerator is the sample median of the error difference sequence

$$\widehat{M}_d = \text{median}(\{d_i\}_{i=1}^N).$$

This value represents the typical accuracy gap between the variant model and the baseline model, with its sign indicating which model has better accuracy.

The denominator is the Median Absolute Deviation (MAD) of the baseline model's error sequence, $\{\varepsilon_i^{(b)}\}_{i=1}^N$. The MAD is a robust measure of statistical dispersion. Denoting the median of the baseline errors as $\widehat{M}_\varepsilon = \text{median}(\{\varepsilon_k^{(b)}\}_{k=1}^N)$, the MAD is defined as:

$$\text{MAD} := \text{median}\left(\left\{|\varepsilon_i^{(b)} - \widehat{M}_\varepsilon|\right\}_{i=1}^N\right).$$

Thus, our effect size measure, the ratio of the median difference to the baseline's MAD,

$$\text{Effect Size} = \frac{\widehat{M}_d}{\text{MAD}},$$

quantifies the magnitude of the accuracy difference relative to the baseline's own variability. This provides a standardized and interpretable metric of the accuracy difference.

C.5 Behavioral Correlation of the Models

Finally, to assess the behavioral similarity between the variant model and the baseline modified DeepONet model, we compute Spearman's rank correlation coefficient ρ [Hollander

et al. 2013; Spearman 1904]. This non-parametric measure evaluates the strength and direction of the monotonic relationship between the two models' error profiles.

Given the error sequences $\{\varepsilon_i^{(v)}\}_{i=1}^N$ and $\{\varepsilon_i^{(b)}\}_{i=1}^N$, each is converted into its corresponding rank sequence, denoted $\{\hat{R}_i^{(v)}\}_{i=1}^N$ and $\{\hat{R}_i^{(b)}\}_{i=1}^N$. Spearman's ρ is then calculated as the Pearson correlation coefficient applied to these rank sequences. A high positive correlation ($\rho \approx 1$) indicates that the models tend to perform well or poorly on the same test cases, suggesting similar underlying behavior.

C.6 Statistical Analysis Results

The results of the rigorous statistical analysis process outlined earlier in this section are summarized in Table C1.

Table C1: Statistical comparison of selected variants against the modified DeepONet across different equations.

Equation	Advection	Diffusion–Reaction	Burgers’ ($\nu = 10^{-2}$)	Burgers’ ($\nu = 10^{-3}$)
Variant	BxTG	TL	TF	TF
Percentage (%)	57.00	64.90	20.40	47.80
Equivalence Margin (%)	0.10	0.02	0.01	0.06
$p^{(\text{lower})}$	0.00	0.0027	0.00	0.00
$p^{(\text{upper})}$	0.00	0.00	1.00	0.00
Equivalent or Not	Yes	Yes	No	Yes
Median Difference (%)	−0.0063	−0.0127	0.0248	0.0115
Glass’s Δ	–	–	0.397	–
Spearman’s ρ	0.993	0.769	0.858	0.869
Equation	Burgers’ ($\nu = 10^{-4}$)		KdV	
Variant	TF	BxTF	BxTG	
Percentage (%)	68.80	83.00	56.00	
Equivalence Margin (%)	0.86	0.86	0.04	
$p^{(\text{lower})}$	1.00	1.00	0.823	
$p^{(\text{upper})}$	0.00	0.00	0.00	
Equivalent or Not	No	No	No	
Median Difference (%)	−3.3255	−4.7989	−0.0152	
Glass’s Δ	−0.393	−0.568	−0.054	
Spearman’s ρ	0.515	0.542	0.860	

D Symbols & Notation

Table D1 summarizes the main symbols and notation used in this work.

Table D1: Summary of the main symbols and notation used in this work.

Notation	Description
t	Temporal query coordinate
n_t	Number of time steps in solution dataset
$\mathbf{x} \in \mathbb{R}^d$	Spatial query coordinate
n_x	Number of spatial points in solution dataset
\mathbf{y}	Trunk input of “vanilla” DeepONet
\mathbf{u}	Input function (branch input of “vanilla” DeepONet)
$\{\mathbf{x}_i\}_{i=1}^m$	m sensor spatial locations of input functions \mathbf{u}
$\hat{\mathbf{u}}_\Lambda = (\hat{u}_k)_{k \in \Lambda}$	A truncated set of Fourier coefficients of \mathbf{u}
\mathbf{s}	A solution to a parametric PDE
G	Solution operator
G^θ	Approximation of a solution operator
θ	All trainable parameters
PDE	Partial differential equation
GRF	Gaussian random field
NTK	Neural tangent kernel
CK	Conjugate kernel
BRDR	balanced-residual-decay-rate
$(b_1, b_2, \dots, b_w)^\top \in \mathbb{R}^w$	Branch output
$(\gamma_1, \gamma_2, \dots, \gamma_w)^\top \in \mathbb{R}^w$	Trunk output
D	Diffusion coefficient of Diffusion–Reaction equation
k	Reaction rate of Diffusion–Reaction equation
ν	Viscosity of Burgers’ equation
δ	Dispersion parameter of KdV equation

References

Boullé, Nicolas and Alex Townsend

- 2024 “A mathematical guide to operator learning”, in, *Numerical analysis meets machine learning*, ed. by Siddhartha Mishra and Alex Townsend, Handbook of Numerical Analysis, Elsevier, vol. 25, chap. 3, pp. 83–125,
DOI: [10.1016/bs.hna.2024.05.003](https://doi.org/10.1016/bs.hna.2024.05.003).

Chen, Junfeng and Kailiang Wu

- 2024 “Positional knowledge is all you need: position-induced transformer (PiT) for operator learning”, in *Proceedings of the 41st International Conference on Machine Learning*, ICML’24, JMLR.org, pp. 7526–7552,
URL: <https://dl.acm.org/doi/abs/10.5555/3692070.3692363>.

Chen, Wenqian, Amanda A. Howard and Panos Stinis

- 2025 “Self-adaptive weights based on balanced residual decay rate for physics-informed neural networks and deep operator networks”, *Journal of Computational Physics*, article 114226,
DOI: [10.1016/j.jcp.2025.114226](https://doi.org/10.1016/j.jcp.2025.114226).

Cox, Stephen M. and Paul C. Matthews

- 2002 “Exponential time differencing for stiff systems”, *Journal of Computational Physics*, vol. 176, issue 2, pp. 430–455,
DOI: [10.1006/jcph.2002.6995](https://doi.org/10.1006/jcph.2002.6995).

E, Weinan and Bing Yu

- 2018 “The deep Ritz method: a deep learning-based numerical algorithm for solving variational problems”, *Communications in Mathematics and Statistics*, vol. 6, issue 1, pp. 1–12,
DOI: [10.1007/s40304-018-0127-z](https://doi.org/10.1007/s40304-018-0127-z).

Evans, Lawrence C

- 2022 *Partial Differential Equations*, 2nd ed., Graduate Studies in Mathematics, American mathematical society, vol. 19,
URL: <https://bookstore.ams.org/gsm-19-r>.

Frisch, U. and J. Bec

- 2001 “Burgulence”, in, *New trends in turbulence turbulence: nouveaux aspects*, ed. by M. Lesieur, A. Yaglom and F. David, Springer Berlin Heidelberg, Berlin, Heidelberg, pp. 341–383,
DOI: [10.1007/3-540-45674-0_7](https://doi.org/10.1007/3-540-45674-0_7).

Glass, Gene V.

- 1976 “Primary, secondary, and meta-analysis of research”, *Educational Researcher*, vol. 5, issue 10, pp. 3–8,
URL: <https://www.jstor.org/stable/1174772>.

Han, Jiequn, Arnulf Jentzen and Weinan E

- 2018 “Solving high-dimensional partial differential equations using deep learning”, *Proceedings of the National Academy of Sciences*, vol. 115, issue 34, pp. 8505–8510,
DOI: [10.1073/pnas.1718942115](https://doi.org/10.1073/pnas.1718942115).

- Hao, Zhongkai, Zhengyi Wang, Hang Su, Chengyang Ying, Yinpeng Dong, Songming Liu, Ze Cheng, Jian Song and Jun Zhu
 2023 “GNOT: a general neural operator transformer for operator learning”, in *Proceedings of the 40th International Conference on Machine Learning*, ICML’23, JMLR.org, pp. 12556–12569,
 URL: <https://dl.acm.org/doi/10.5555/3618408.3618917>.
- Hesthaven, Jan S, Gianluigi Rozza and Benjamin Stamm
 2016 *Certified Reduced Basis Methods for Parametrized Partial Differential Equations*, Springer Briefs in Mathematics, Springer, vol. 590,
 DOI: [10.1007/978-3-319-22470-1](https://doi.org/10.1007/978-3-319-22470-1).
- Hollander, Myles, Douglas A. Wolfe and Eric Chicken
 2013 *Nonparametric Statistical Methods*, John Wiley & Sons,
 DOI: [10.1002/9781119196037](https://doi.org/10.1002/9781119196037).
- Howard, Amanda A., Sarah H. Murphy, Shady E. Ahmed and Panos Stinis
 2025 “Stacked networks improve physics-informed training: applications to neural networks and deep operator networks”, *Foundations of Data Science*, vol. 7, issue 1, pp. 134–162,
 DOI: [10.3934/fods.2024029](https://doi.org/10.3934/fods.2024029).
- Iserles, Arieh
 2008 *A First Course in the Numerical Analysis of Differential Equations*, 2nd ed., Cambridge Texts in Applied Mathematics, Cambridge University Press,
 DOI: [10.1017/CB09780511995569](https://doi.org/10.1017/CB09780511995569).
- Kissas, Georgios, Jacob H Seidman, Leonardo Ferreira Guilhoto, Victor M Preciado, George J Pappas and Paris Perdikaris
 2022 “Learning operators with coupled attention”, *Journal of Machine Learning Research*, vol. 23, issue 215, pp. 1–63,
 URL: <https://www.jmlr.org/papers/v23/21-1521.html>.
- Kovachki, Nikola, Zongyi Li, Burigede Liu, Kamyar Azizzadenesheli, Kaushik Bhattacharya, Andrew Stuart and Anima Anandkumar
 2023 “Neural operator: learning maps between function spaces with applications to PDEs”, *Journal of Machine Learning Research*, vol. 24, issue 89, pp. 1–97,
 URL: <https://www.jmlr.org/papers/v24/21-1524.html>.
- Krishnapriyan, Aditi, Amir Gholami, Shandian Zhe, Robert Kirby and Michael W Mahoney
 2021 “Characterizing possible failure modes in physics-informed neural networks”, in *Proceedings of the 35th International Conference on Neural Information Processing Systems*, NIPS’21, Curran Associates, Inc., pp. 26548–26560,
 URL: <https://dl.acm.org/doi/10.5555/3540261.3542294>.

- Li, Zijie, Kazem Meidani and Amir Barati Farimani
 2022 Transformer for partial differential equations' operator learning,
 ARXIV: [2205.13671](#).
- Li, Zongyi, Nikola Kovachki, Kamyar Azizzadenesheli, Burigede Liu, Kaushik Bhattacharya,
 Andrew Stuart and Anima Anandkumar
 2020 Fourier neural operator for parametric partial differential equations,
 ARXIV: [2010.08895](#).
- Lu, Lu, Pengzhan Jin, Guofei Pang, Zhongqiang Zhang and George Em Karniadakis
 2021 "Learning nonlinear operators via DeepONet based on the universal approximation theorem of operators", *Nature Machine Intelligence*, vol. 3, issue 3,
 pp. 218–229,
 DOI: [10.1038/s42256-021-00302-5](#).
- Meuris, Brek, Saad Qadeer and Panos Stinis
 2023 "Machine-learning-based spectral methods for partial differential equations",
Scientific Reports, vol. 13, issue 1, article 1739,
 DOI: [10.1038/s41598-022-26602-3](#).
- Phuong, Mary and Marcus Hutter
 2022 Formal algorithms for transformers,
 ARXIV: [2207.09238](#).
- Qadeer, Saad, Andrew Engel, Amanda Howard, Adam Tsou, Max Vargas, Panos Stinis and
 Tony Chiang
 2023 Efficient kernel surrogates for neural network-based regression,
 ARXIV: [2310.18612](#).
- Quarteroni, Alfio, Andrea Manzoni and Federico Negri
 2015 *Reduced Basis Methods for Partial Differential Equations: An Introduction*,
 Unitext, Springer, vol. 92,
 DOI: [10.1007/978-3-319-15431-2](#).
- Raissi, Maziar, Paris G. Perdikaris and George Em Karniadakis
 2019 "Physics-informed neural networks: a deep learning framework for solving forward
 and inverse problems involving nonlinear partial differential equations", *Journal
 of Computational Physics*, vol. 378, pp. 686–707,
 DOI: [10.1016/j.jcp.2018.10.045](#).
- Schuurmann, Donald J.
 1987 "A comparison of the two one-sided tests procedure and the power approach for
 assessing the equivalence of average bioavailability", *Journal of Pharmacokinetics
 and Pharmacodynamics*, vol. 15, issue 6, pp. 657–680,
 DOI: [10.1007/BF01068419](#).

- Shih, Benjamin, Ahmad Peyvan, Zhongqiang Zhang and George Em Karniadakis
- 2025 “Transformers as neural operators for solutions of differential equations with finite regularity”, *Computer Methods in Applied Mechanics and Engineering*, vol. 434, article 117560,
DOI: [10.1016/j.cma.2024.117560](https://doi.org/10.1016/j.cma.2024.117560).
- Spearman, Charles
- 1904 “The proof and measurement of association between two things”, *The American Journal of Psychology*, vol. 15, issue 1, pp. 72–101,
DOI: [10.2307/1412159](https://doi.org/10.2307/1412159).
- Tan, Lesley and Liang Chen
- 2022 Enhanced DeepONets for modeling partial differential operators considering multiple input functions,
ARXIV: [2202.08942](https://arxiv.org/abs/2202.08942).
- Vaswani, Ashish, Noam Shazeer, Niki Parmar, Jakob Uszkoreit, Llion Jones, Aidan N. Gomez, Łukasz Kaiser and Illia Polosukhin
- 2017 “Attention is all you need”, in *Proceedings of the 31st International Conference on Neural Information Processing Systems*, NIPS’17, Curran Associates, Inc., pp. 6000–6010,
URL: <https://dl.acm.org/doi/10.5555/3295222.3295349>.
- Venturi, Simone and Tiernan Casey
- 2023 “SVD perspectives for augmenting DeepONet flexibility and interpretability”, *Computer Methods in Applied Mechanics and Engineering*, vol. 403, article 115718,
DOI: [10.1016/j.cma.2022.115718](https://doi.org/10.1016/j.cma.2022.115718).
- Wang, Sifan and Paris Perdikaris
- 2023 “Long-time integration of parametric evolution equations with physics-informed DeepONets”, *Journal of Computational Physics*, vol. 475, article 111855,
DOI: [10.1016/j.jcp.2022.111855](https://doi.org/10.1016/j.jcp.2022.111855).
- Wang, Sifan, Hanwen Wang and Paris Perdikaris
- 2021 “Learning the solution operator of parametric partial differential equations with physics-informed DeepONets”, *Science Advances*, vol. 7, issue 40, article eabi8605,
DOI: [10.1126/sciadv.abi8605](https://doi.org/10.1126/sciadv.abi8605).
- 2022 “Improved architectures and training algorithms for deep operator networks”, *Journal of Scientific Computing*, vol. 92, issue 2, article 35,
DOI: [10.1007/s10915-022-01881-0](https://doi.org/10.1007/s10915-022-01881-0).

Wang, Sifan, Xinling Yu and Paris Perdikaris

- 2022 “When and why PINNs fail to train: a neural tangent kernel perspective”, *Journal of Computational Physics*, vol. 449, article 110768,
DOI: [10.1016/j.jcp.2021.110768](https://doi.org/10.1016/j.jcp.2021.110768).

Wellek, Stefan

- 2010 *Testing Statistical Hypotheses of Equivalence and Noninferiority*, 2nd ed., Chapman and Hall/CRC, New York,
DOI: [10.1201/EBK1439808184](https://doi.org/10.1201/EBK1439808184).

Wilcox, Rand R.

- 2011 *Introduction to Robust Estimation and Hypothesis Testing*, Academic press,
DOI: [10.1016/C2010-0-67044-1](https://doi.org/10.1016/C2010-0-67044-1).

Wilcoxon, Frank

- 1945 “Individual comparisons by ranking methods”, *Biometrics Bulletin*, vol. 1, issue 6, pp. 80–83,
DOI: [10.2307/3001968](https://doi.org/10.2307/3001968).

Williams, Emily, Amanda Howard, Brek Meuris and Panos Stinis

- 2024 What do physics-informed DeepONets learn? Understanding and improving training for scientific computing applications,
ARXIV: [2411.18459](https://arxiv.org/abs/2411.18459).

Yu, Xinling, Sean Hooten, Ziyue Liu, Yequan Zhao, Marco Fiorentino, Thomas Van Vaerenbergh and Zheng Zhang

- 2024 Separable operator networks,
ARXIV: [2407.11253](https://arxiv.org/abs/2407.11253).

Zhu, Yameng, Jingrun Chen and Weibing Deng

- 2024 R-adaptive DeepONets: learning solution operators for PDEs with discontinuous solutions using an R-adaptive strategy,
ARXIV: [2408.04157](https://arxiv.org/abs/2408.04157).